Post-buckling damage tolerance of welded omega-stiffened thermoplastic panels with initial damage

van Dooren, Kevin; Bisagni, Chiara

Important note
To cite this publication, please use the final published version (if applicable).
Please check the document version above.

Post-buckling damage tolerance of welded omega-stiffened thermoplastic panels with initial damage

Kevin van Dooren, Chiara Bisagni *

Delft University of Technology, Faculty of Aerospace Engineering, Delft, The Netherlands

ARTICLE INFO

ABSTRACT

Welded omega-stiffened panels made of thermoplastic carbon composite with initial damage in the conduction welded joint are analysed and tested to investigate the damage tolerance in post-buckling. Finite element analyses are performed, using the virtual crack closure technique to investigate skin-stringer separation for both the pristine welded joint and joints with initial damage. A sensitivity study is executed for the initial damage size and location with different geometrical imperfections. Four omega-stiffened panels are tested, of which three have initial damage consisting of a foil at the welded skin-stringer interface. During the test, digital image correlation is used to measure the panels' deformation to determine the evolution of the buckling shape and the interaction with the initial damage. A high-speed camera is placed on the stringer side of the panel to capture the final failure. The panels fail in post-buckling when skin-stringer separation occurs, starting from the initial damage. The finite element analysis is able to predict the overall structural behaviour well, with conservative failure load predictions for panels with initial damage in the middle stringer. Although the initial buckling shape is predicted well, the buckling shape evolution at higher loads is difficult to predict.

1. Introduction

Composite materials are increasingly used in the aeronautical field because of their performance-to-weight ratio. The structures commonly used in aeronautics consist of thin-walled designs with stiffening elements, such as the stiffened skin of a fuselage or wing. These structures are often subjected to compression loads, which leads to buckling, and have been shown to withstand load far into the post-buckling field [1,2]. However, these structures are vulnerable to damage during manufacturing, in-service or maintenance, from which composite structures are more likely to sustain damage than metallic structures. The damage can occur internally and not show signs of damage during a visual inspection. This increases the concerns about allowing the structures to operate in the post-buckling field due to the complex nature of post-buckling behaviour and possible interaction with internal damages. Considerable weight savings can be achieved by allowing post-buckling, which requires an increased understanding of the damage tolerance of composite structures in post-buckling.

Stiffened structures in post-buckling exhibit high out-of-plane deformations of the skin, which leads to skin-stringer separation as the common failure mode due to the high interface stresses between skin and stringer [3]. Skin-stringer separation is a widely researched phenomenon on thermoset composites [4–6] and, to a lesser extent, thermoplastic composites [1,2]. The research on skin-stringer separation

can be divided into the structural levels it is researched on, such as single-stringers and multi-stringer panel level, and the stringer design.

The damage tolerance of composite structures in post-buckling was investigated by Bisagni et al. [7]. Single-stringer compression specimens with omega stringer were designed to show structural behaviour representative of a multi-stringer panel. Bisagni and Dávila [8] further investigated the single-stringer compression specimens, with geometrical imperfections measurements and digital image correlation was used during the test to determine the buckling shape. Action and Leone [9] analysed and tested a multi-stringer panel with omega stringers and Teflon inserts to validate the CompDam material model. The panel failed due to skin-stringer separation in post-buckling, which showed stable damage growth before it became unstable and the panel collapsed. Mo et al. [10] presented an experimental and numerical study on curved multi-stringer panels with omega stringers investigating the buckling and post-buckling behaviour. The study focussed on the effect of curvature, stringer spacing and skin thickness on the buckling behaviour and the prediction by Finite Element analysis. Feng et al. [11] studied the effect of impact damage positions on the buckling and post-buckling behaviour of stiffened panels with I-stringers. Panels were subjected to impact to create Barely Visible Impact Damage in different positions. It was seen that the impact damage had little influence on

---

the buckling load, compared to a pristine panel, but the failure load decreased up to 10%. Sepe et al. [12] tested and analysed two-stringer panels to investigate the residual strength after low-velocity impact and with a cut-out. The multiple impacts and cut-out lowered the ultimate strength of the panel by approximately 30%. Stiffened panels made of thermoplastic composite were tested in compression after impact by Ishikawa and Matsushima [13]. Two single-stringer hat-stiffened panels were impacted at a different energy level, resulting in delaminations between skin and stringer of approximately 18 and 900 mm^2, that lead to a difference of 20% in compression after impact strength.

Blade-stiffened panels in pristine condition and with initial damage were analysed and tested in post-buckling by Orifici et al. [14]. Two different panel designs were tested, with panel lengths of 400 and 500 mm and an initial damage length of 80 and 105 mm, respectively. The initial damage reduced the failure load up to approximately 50% in post-buckling. Riccio et al. [15] introduced a numerical procedure which utilizes both the Virtual Crack Closure Technique (VCCT) and the Cohesive Zone Method (CZM) to model skin-stringer separation. The numerical results are compared to the experimental data of Orifici et al. [14], and showed good correlation. Bertolini et al. [16,17] compared the modelling of separation by VCCT and CZM on non-specific specimen level and then applied VCCT on element and panel level because of its computational efficiency. The computational time differed by one order of magnitude on specimen level, and CZM was therefore considered unsuitable for industrial applications at the higher structural level.

The sensitivity of stiffened panels with blade stringers to the damage size, width, location and the number of initial damage locations was numerically investigated by Ji et al. [18]. The damage size had the largest effect on the final failure load, with a debond length of 10% of the panel length, causing a 25% reduction of the final failure load. The sensitivity to the initial damage size and location of stiffened panels with omega stringers was numerically investigated by Yetman et al. [19]. The damage size influenced both the buckling load and failure load, while the damage location only influenced the failure load and not the buckling load.

This research focuses on the damage tolerance of thermoplastic stiffened structures with welded joints. Thermoplastic composites show excellent promise for aeronautical structures regarding sustainability and cost-savings while also increasing damage tolerance due to the high toughness [20]. They offer new ways of manufacturing composite materials for out-of-autoclave processes, such as thermoforming, thermoplastic welding [21], in-situ consolidation [22], and in-autoclave co-consolidation [23].

The structures investigated in this research represent components of the thermoplastic multi-functional fuselage demonstrator of the STUNNING project [2,24]. This project developed the required technologies for manufacturing the fuselage demonstrator, which consists of techniques such as compression moulding, press-forming and conduction welding. This paper conducts a combined numerical and experimental investigation to evaluate the damage tolerance of the conduction welded joint between skin and omega stringer in the post-buckling field. The higher toughness and new manufacturing technologies of thermoplastics can contribute greatly to the push for composite primary structures and advance towards structures designed for post-buckling below ultimate load.

In this paper, omega-stiffened thermoplastic panels are analysed and tested to investigate the damage tolerance of the conduction welded joint. Three panels have initial damage, and one panel is in a pristine state. The panels are manufactured by project partners NLR — Netherlands Aerospace Centre and GKN Fokker. The initial damage involves a foil inserted at the skin-stringer interface before welding. The numerical analyses are done with Abaqus and use the Virtual Crack Closure Technique to model skin-stringer separation for pristine joints and joints with initial damage. The analyses are executed to predict the behaviour of the test panels, with initial geometrical imperfections accounted for, and for a sensitivity study on damage size and location. The four panels are tested until they collapse.

Table 1
CF/LM-PAEK Toray CETEX TC1225 material properties [25].

E_{11} [MPa]	E_{22} [MPa]	v_{12} [–]	G_{12} [MPa]	F_1^t [MPa]	F_1^c [MPa]	F_2^t [MPa]	F_2^c [MPa]	F_{12} [MPa]
116800	9100	0.36	4100	2442	1250	94	212	99

Table 2
Layups of the welded omega-stiffened thermoplastic panel.

Name	Layup	Thickness (mm)
Skin	$[-45/45/90/0/90/0]_s$	2.208
Stringer	$[45/0/-45/0/\underline{90}]_s$	1.656

2. Welded omega-stiffened thermoplastic panels

The welded omega-stiffened thermoplastic panels are designed to show structural behaviour similar to the STUNNING fuselage [2]. They have three stringers, to allow for bay buckling on both sides of the middle stringer and achieve a deformation and loading similar to a fuselage section. The stringer pitch is equal to the stringer pitch of the keel section of the STUNNING fuselage, 212 mm, which results in a total width of 556 mm, as reported in Fig. 1. The panels are 490 mm long, which is the maximum welding length at the time of production, with the panel's loading edges trimmed.

The omega stringer is 132 mm wide, 30 mm in height and has a web-cap angle of 125°, as reported in Fig. 2. The flange width is 28.7 mm, and the cap width is 30 mm.

The panels are made of CF/LM-PAEK material, and the properties used are reported in Table 1 [25], with 1 and 11 notation for properties in fibre direction and 2 and 22 notation for properties transverse to the fibre. The nominal ply thickness is 0.184 mm, and the layups of the skin and stringer are reported in Table 2. The stacking direction of the plies coincides with the Z-axis, and the 0° and 90° directions coincide with the X and Y-axis, respectively, according to the coordinate system reported in Fig. 1.

Four omega-stiffened panels are manufactured. The skin is manufactured by project partner NLR — Netherlands Aerospace Centre. The skin is laid up by automatic tape laying and then consolidated in an autoclave. The stringers are joined to the skin with conduction welding by project partner GKN Fokker. The conduction welding process involves a heating element applying pressure and heat on top of the stringer flange, which melts the material and joins the skin and stringer. The weld is approximately in the middle of the stringer flange, with small unwelded regions on both sides of the weld, as reported in Fig. 2. The weld width at the interface is approximately 18 mm. The initial damage is created by inserting a foil between the skin and the stringer flange, which prevents this area from being welded. The panels are received from the project partners as reported in Fig. 3(a). The panels are then prepared for testing in several steps. They are trimmed, followed by the casting of potting to both ends of the panel for load introduction. Then the loading faces of the panels are machined to minimize loading imperfections. The following steps are to attach strain gauges and wiring, as shown in Fig. 3(b). The panels have 10 strain gauges attached, of which the locations are reported in Fig. 4, 135 mm from the bottom loading plane. The strain gauges are on top of the cap and the bottom of the skin underneath each stringer. There are two strain gauges attached back-to-back in the bays. The strain measurements are used for load distribution and redistribution due to phenomena such as buckling and failure, and also for loading imperfections. The last step is to paint the panels in matt white, followed by black speckles, for digital image correlation.

3. Numerical analysis of welded omega-stiffened thermoplastic panels with initial damage

The numerical analyses are executed to study the buckling, failure behaviour and damage tolerance of the panels with Abaqus 2021 [26].
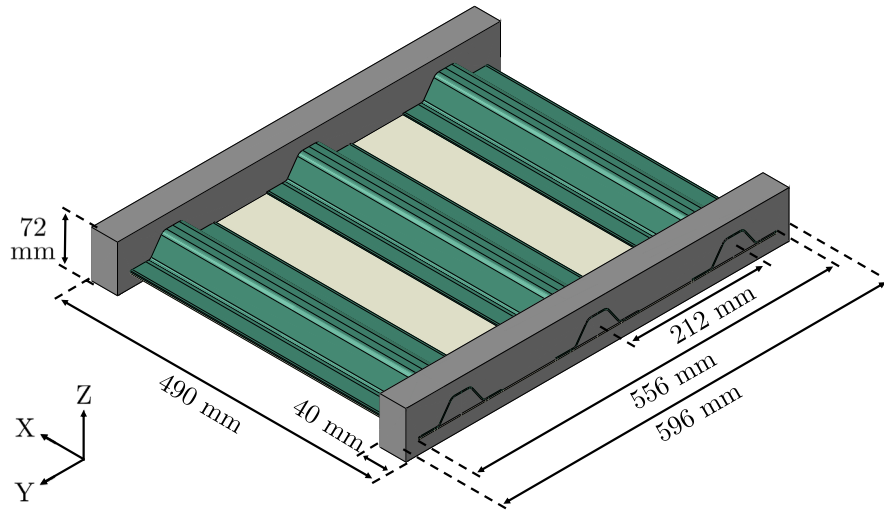
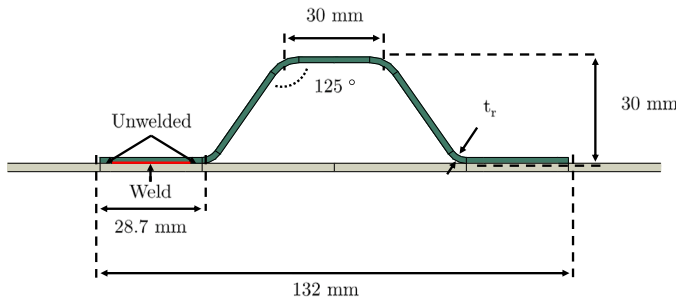**Fig. 1.** Welded omega-stiffened thermoplastic panel.

Fig. 2. Omega stringer geometry and weld.

Table 3
Fracture properties of skin-stringer interface [27].

G_{IC} [kJ/m^2]	G_{IIC} [kJ/m^2]	G_{IIIC} [kJ/m^2]	η [–]
0.969	1.719	1.719	2.284

3.1. Analysis methodology

The panels are analysed with a dynamic implicit analysis and non-linear geometry enabled. The analysis time is 1 s with a minimum time-step of 1e-08 s and a maximum and initial time-step of 0.01 s. Load is applied with displacement boundary conditions on two reference nodes. The reference nodes are placed at each loading plane, as reported in Fig. 5(a), and rigid body ties are used between the reference nodes and the loading plane. One reference node is clamped, except in the longitudinal direction, for which 2.5 mm of displacement is applied. The other reference node is clamped. The boundary conditions and the time-step result in a displacement rate of 2.5 mm/s.

The mesh size of the laminated sections is 2.5 mm, which is based on a mesh convergence study. The mesh of the skin and stringer is reported in Fig. 5(b). The potting material has a variable mesh size, between 2.5 and 10 mm. The potting mesh starts fine where it joins to the laminated sections, and becomes courses in an outwards direction. The laminated sections are modelled with continuum shells (SC8R), and the potting is modelled with reduced integration solid elements (C3D8R) for improved computational efficiency.

The laminated sections and the potting are joined with shared nodes in the potting region. The skin and stringer between the potted sections are joined with the Virtual Crack Closure Technique (VCCT), to resemble the welded joint as reported in Fig. 5(b).

In this study, VCCT is utilized for both panels in a pristine state and with initial damage, with a weld width of 18 mm. The VCCT method is normally limited to structures with initial damage due to the pre-crack requirement. However, the weld has small unwelded regions on both sides of the weld, as shown in Fig. 2, allowing VCCT to be used
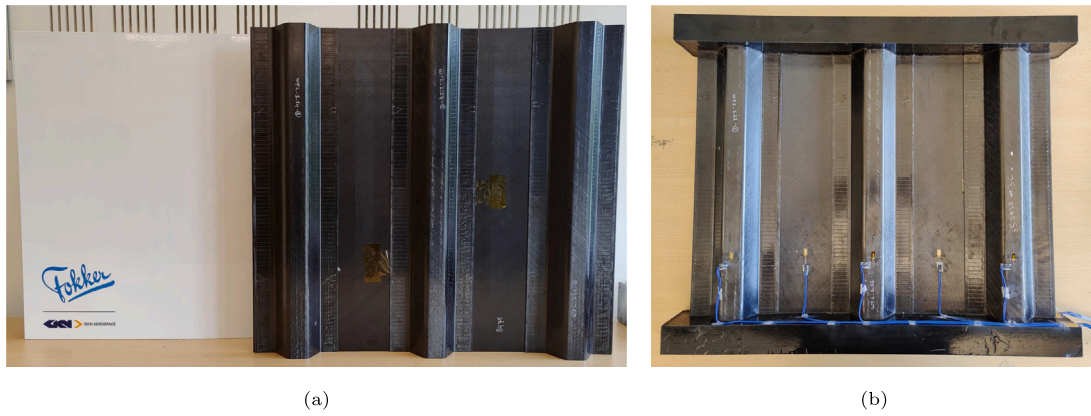
for pristine welded joints. This results in a relatively efficient analysis for a panel-level structure due to the courser mesh allowance of VCCT compared to other methods. In this model, skin-stringer separation can only occur at the interface between skin and stringer, as reported in Fig. 5(b), and cannot grow into the laminates, to limit the complexity of the model and analysis. Also, due to the unwelded region on both sides, it is less likely that separation will migrate.

In the VCCT definition, the skin side is assigned as the slave surface and the stringer side as the master surface, in combination with node-to-surface discretization. Contact stabilization is used with a factor of 1e-4. The fracture tolerance is set to the default value of 0.2, and the unstable crack growth tolerance is set to 1. The Benzeggagh–Kenane (BK) criterion is used to model mode-mixity, which is reported in Eq. (1). To determine when fracture occurs, VCCT calculates the critical equivalent strain energy release rate G_{equivC} using the BK criterion and the equivalent energy release rate with Eq. (2). When $G_{equivC} \geq G_{equiv}$, fracture occurs. The required fracture toughness of the interface, G_{IC}, G_{IIC}, G_{IIIC} and the BK parameter are based on a similar material from literature, AS4/PEEK [27], of which the matrix is of the same polyaryletherketone polymer family. The properties are reported in Table 3. The assumption is made that G_{IIC} and G_{IIIC} are equivalent. G_I, G_{II} and G_{III} are the strain energy release rates for the three different modes, and are calculated based on nodal displacements and forces.

The analysis incorporates first-ply failure criteria to determine if material failure occurs before skin-stringer separation.

$$G_{equivC} = G_{IC} + (G_{IIC} - G_{IC}) \left(\frac{G_{II} + G_{III}}{G_I + G_{II} + G_{III}} \right)^{\eta} \tag{1}$$

$$G_{equiv} = G_I + G_{II} + G_{III} \tag{2}$$

The analysis of the panels can include imperfections that are measured from the panels. The flowchart for including the imperfections is reported in Fig. 6. The chart starts out with the panel model that is created in Abaqus, and the measured imperfections. The measured imperfection is then interpolated onto the mesh with a python script. The next step in this script is to translate the interpolated imperfection into a displacement field representing the imperfection. This displacement field is then used in a linear analysis to deform the panel to the

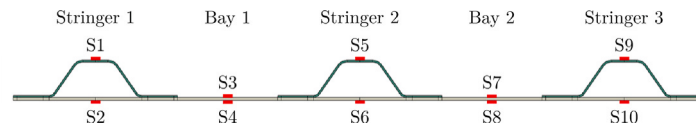**Fig. 3.** Omega-stiffened panels: (a) as received; (b) with potting and strain gauges.
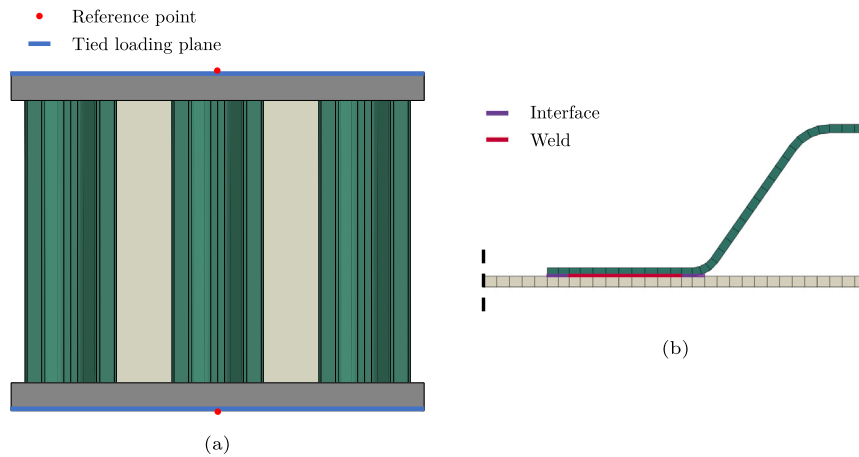

Fig. 4. Strain gauge locations.

Fig. 5. Model details: (a) reference point placement; (b) mesh cross-section.

imperfect shape, from which a node-file is the output. This node-file includes the imperfection, without the internal stresses. The last step is the dynamic implicit analysis, which uses the panel model and the imported node file to include the imperfection.

3.2. Effect of damage size and location

This section focuses on the analysis of panels with different damage sizes and damage locations. The first study considers the damage size of an initial damage in the centre of the panel, as shown in Fig. 7(a). The considered damage sizes are reported in Table 4. The results of the study are reported in terms of the initiation load and the final failure load. Initiation is considered the start of skin-stringer separation, and final failure is considered when unstable separation leads to panel collapse.

The initiation load and failure load for a panel with one initial damage of different sizes are reported in Fig. 8(a). The panel has a low sensitivity to initial damage sizes of 10 and 25 mm, and for a damage size of 40 mm both the initiation and final failure load drop considerably. A buckling shape change most likely causes this drop. The panel starts out with three half-waves in the bays, reported in Fig. 9(a), and the panel with a damage size of 40 mm presents a gradual

shape change to four half-waves, reported in Fig. 9(c). A damage size of 25 mm and below did not show this buckling shape change. The initiation load drops further for larger damage sizes, while the failure load does not go below 230 kN for the damage sizes in this study. Based on these results, it is chosen to use a 40 mm damage size for the test panels, as reported in Fig. 10(a). This damage size presents a considerable drop in final failure load, while there is still a margin between the buckling load of approximately 170 kN and the initiation load of 230 kN. Since the strength of the welded joint is unknown at the time of the design, a conservative damage size is deemed best.

The second study considers the location of the initial damage, for a panel with one initial damage and a panel with two initial damages, both for a damage size of 40 mm. The location is defined as the offset between the panel's centre and the damage's centre, as reported in Fig. 7 (b–c). The study considers one initial damage (Fig. 7(b)) and two initial damages, where the first damage in the right flange will remain in the centre, and the second damage in the left flange will be offset (Fig. 7(c)). The damage offset range of the study is reported in Table 4.

The initiation load and failure load for a panel with one and two initial damages at different locations are reported in Fig. 8(b). For panels with one initial damage, the initiation load is similar for offsets of 0 and 22 mm, and then for higher offsets the initiation load increases.
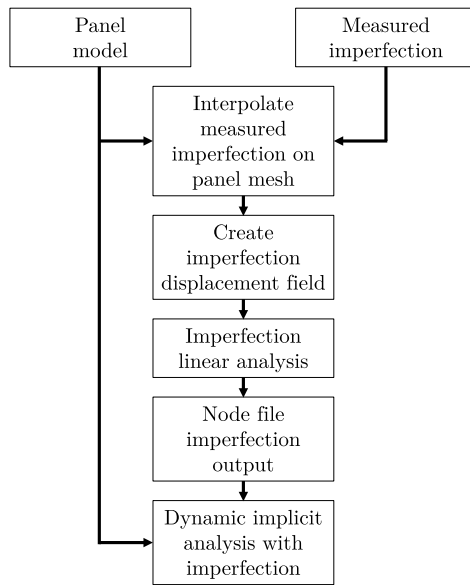
Fig. 6. Flowchart for including imperfections in the analysis.

Table 4
Sensitivity study parameters.

Damage size [mm]	Damage offset [mm]
0	0
10	22
25	44
40	66
55	88
70	110
85	132
100	154

This is caused by differences in the buckling shape evolution. The panels have an initial three half-wave buckling shape, as reported in Fig. 9(a), that changes to four half-waves in one bay for 0 and 22 mm offset, as reported in Fig. 9(b). Higher offsets do not exhibit this buckling shape change. The initiation load does go down between 44 and 110 mm offset, which seems to be caused by the relative position of the damage w.r.t. the outward half-wave being more critical for separation. The failure load is lowest for 0 mm offset, for higher offsets it plateaus at approximately 270 kN. An offset of 0 mm is chosen for the test panel with one initial damage, which is reported in Fig. 10(a).

The panel with two initial damages shows an initiation load of approximately 230 kN for 0, 22 and 44 mm of offset, and increases to approximately 255 kN know for an offset of 66 mm. This difference is caused by the change in buckling shape from three to four half-waves in both bays, as reported in Fig. 9(c), and four half-waves seems to be more critical. The failure load is approximately 270 kN for all cases, which seems to be dominated by a certain amount of separated area after which separation becomes unstable and the panels collapse. Offsets of 88, 110 and 132 mm present similar behaviour in terms of initiation load, but the case of 110 mm is deemed to be most interesting, as the separation starts at the damage in the middle, while the opposite flange also starts to separate in the middle of the panel which grows towards the second initial damage. This interaction is considered interesting, while it has a low risk of the initial damages quickly causing tunnelling behaviour, and far enough from the potting to minimize the influence of boundary conditions. Therefore, an offset of 110 mm is chosen for the panel with two initial damages, as reported in Fig. 10(b).

The last configuration has one initial damage of 40 mm in the side stringer, as reported in Fig. 10(c). This allows to study the effect of initial damage in different stringers.

4. Test setup and panels measurements

The panels are tested in compression until failure with an MTS test machine at Delft University of Technology. The test machine is capable of 3500 kN in tension and compression, and the configuration with the adjustable compression plate is capable of 1300 kN.

The test setup is reported in Fig. 11 from the (a) stringer side and (b) skin side of the panel. The panels are positioned in the test machine and a preload of 2 kN is applied to keep the panel in place. The test

is then executed with a loading rate of 0.1 mm/min. and the loading stops automatically after failure.

Two DIC systems measure the deformation field, with one system on each side of the test setup. The DIC systems have 5 MP cameras, and the post-processing software is VIC3D 8.

The longitudinal displacement of the compression plate is measured by three Laser Displacement Sensors (LDS). Two LDS are placed next to the potting ends, and one is placed out-of-plane on the corner of the plate, which allows to determine if loading imperfections occur.

All mentioned measurement systems record every 3 s, which results in approximately 500 data points per test for a pristine panel. Three cameras are used to capture the test, with two cameras on the stringer side to capture the buckling and skin-stringer separation behaviour and one camera on the skin side.

Final failure of the panels is captured by a high-speed camera which records at 10000 fps. The camera captures the full panel.

The imperfections of the panels are measured. The measurements allow comparing the imperfections between the panels, and a selection of the imperfections will be taken into account in the numerical analysis.

The first imperfection that is measured is the out-of-plane imperfection of the skin, for which DIC is used. The nominal design has a flat skin, and the imperfection is the deviation of the skin w.r.t. a flat plane. The out-of-plane imperfections of all four panels are reported in Fig. 12. All four panels have a similar curved imperfection in the width direction, with a total magnitude of the imperfection ranging from 12.36 mm to 15.88 mm. The imperfection has a counterclockwise skew, probably caused by the layup and the outer -45 ply. The panels are also slightly curved in the longitudinal direction, but it is minimal compared to the imperfection in the width direction. The highest curvature in the width direction is in the welded area, as the imperfection is mostly caused by the local heating of the conduction welding process, which results in thermal stresses.

The skin and stringer laminate thickness is measured with a micrometer. The skin has an average thickness of 2.14 mm, which is thinner than the nominal thickness. The stringers have an average thickness of 1.66 mm, close to the nominal thickness. The bottom radius of the stringer is, however, thinner than nominal, with an approximate thickness of 1.15 mm.

The stringer spacing is measured to determine stringer offset and alignment. Panels 1 and 2 have no considerable offset or misalignment. Panels 3 and 4 have an offset of approximately 1 mm of the middle stringer.

The numerical analysis of the four panels will include a selection of these imperfections, which are: the out-of-plane imperfection, the skin thickness, the thickness of the bottom stringer radius, the middle stringer offset of panels 3 and 4, and finally, the average panel length of 491 mm. The skin thickness is lowered from the nominal thickness to the average measured thickness, and the thickness of the bottom radius of the stringer is made thinner locally. Residual stresses from the manufacturing process are not taken into account.
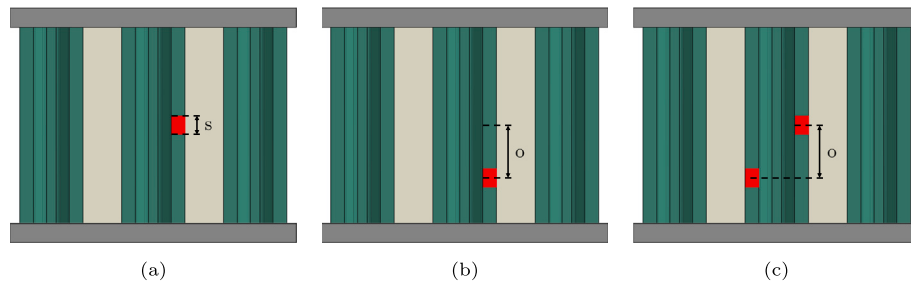
Fig. 7. Panel illustrations of three sensitivity parameters: (a) damage size; (b) damage 1 offset; (c) damage 2 offset.
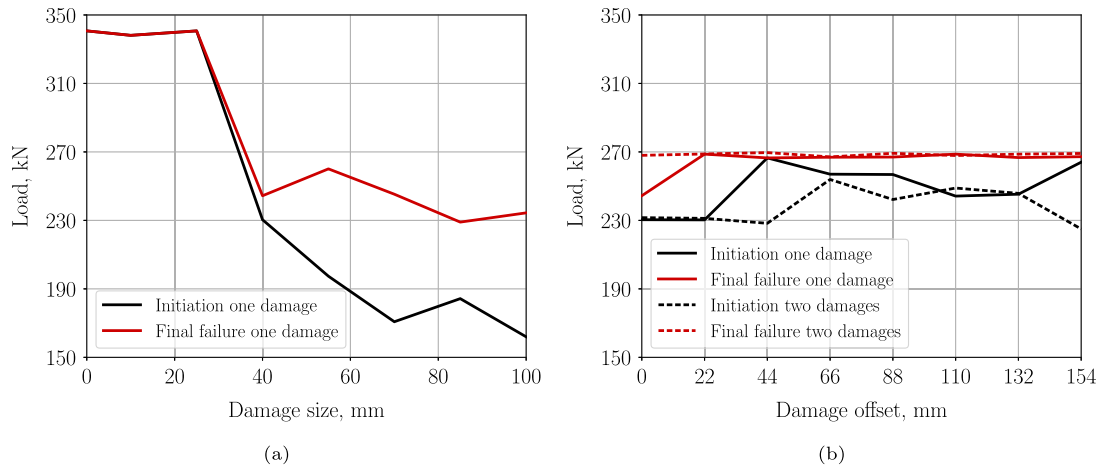

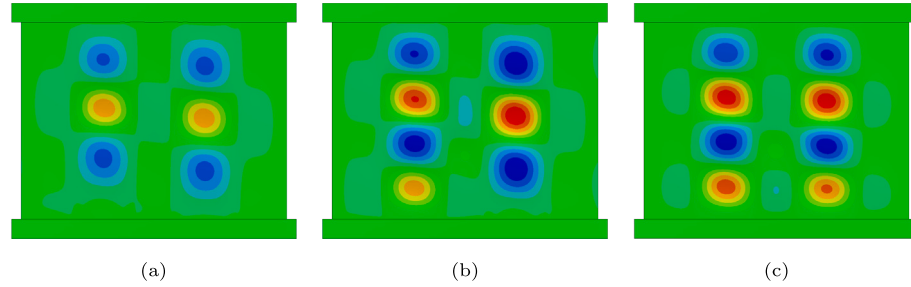**Fig. 8.** Sensitivity study of: (a) damage size; (b) damage offset.

Fig. 9. Buckling shapes: (a) three half-waves; (b) three and four half-waves; (c) four half-waves.
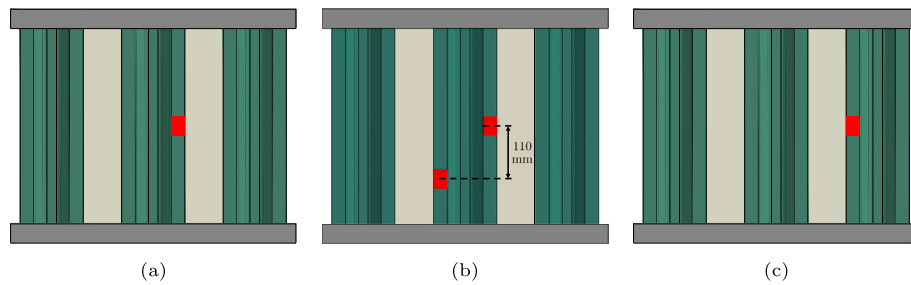

Fig. 10. Panels with initial damage of 40 mm: (a) panel 2; (b) panel 3; (c) panel 4.

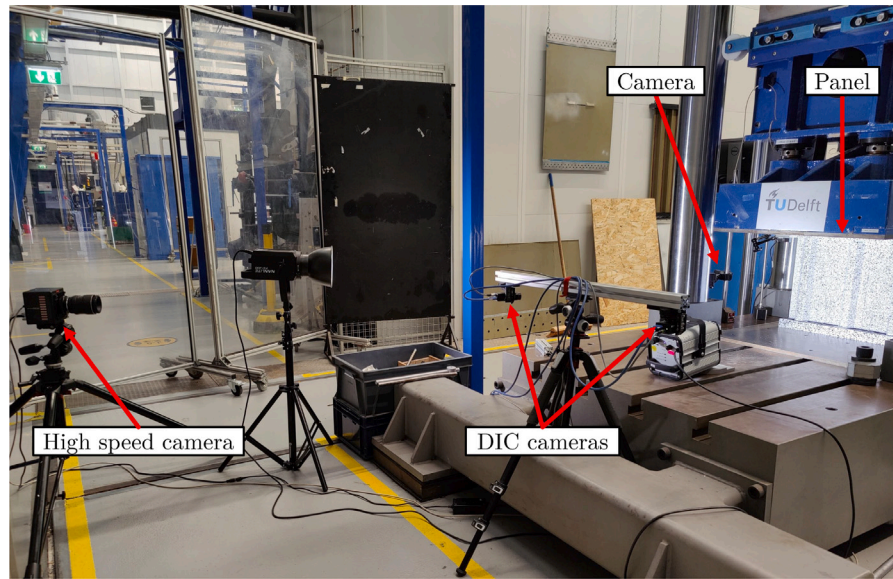## 5. Damage and imperfection sensitivity study

This study considers the interaction between the damage location and size for different geometrical imperfections.

The study is executed for different imperfection amplitudes, as reported in Table 5. The damage size sensitivity study will be done for both panel 1 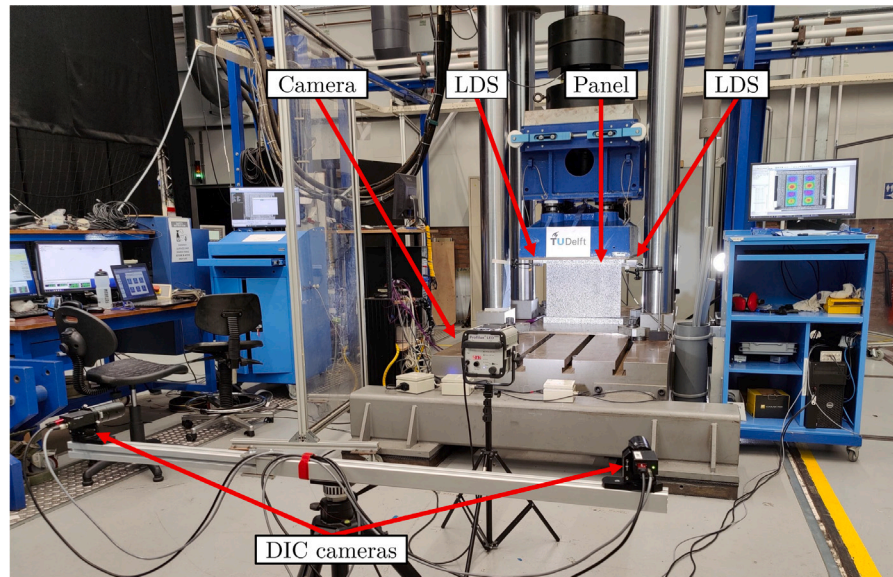and 2 imperfections, which are reported in Fig. 12(a) and (b), respectively, and the damage location sensitivity study for the panel 2 imperfection.

5.1. Damage size sensitivity

The initiation loads for the damage size sensitivity study with panels 1 and 2 geometrical imperfections are reported in Fig. 13(a) and (b),

(a)

(b)

Fig. 11. Test setup seen from: (a) stringer side; (b) skin side.

Table 5

Sensitivity study parameters.

Imperfection amplitude
0
0.5
1
1.5

respectively. For small damage sizes, a higher imperfection amplitude lowers the initiation load, especially for the imperfection of panel 2. At a damage size of 40 mm and larger, the initiation load drops considerably for most cases, except for an imperfection amplitude of 0.5 of panel 2. The initiation load is generally higher for higher imperfections at large damage sizes. This is probably due to the curvature of the imperfection leading to less opening of the initial damage. The average initiation load for a damage size of 40 mm is 275 kN for the imperfection of panel 2, while it is 234 kN for the imperfection of panel 1. This is a decrease in the failure load compared to a pristine panel of 30% and 17% for panels 1 and 2, respectively. The initiation loads drop further for larger damages, with the case of no imperfection presenting the highest sensitivity to the damage. The failure loads of the damage size sensitivity study are reported in Fig. 13(c) and (d), for panels 1 and 2, respectively. When comparing the results to the initiation loads in Fig. 13(a) and (b), it can be concluded that for damage sizes of 40 mm and smaller, the panels show final failure at or shortly after the initiation of skin-stringer separation. At larger damage sizes, the failure load increases for the imperfection of panel 2 and an amplitude of 1 and 1.5. This is also seen for the imperfection amplitude of 1 of panel 1, while imperfection amplitudes of 0.5 and 1.5 have varying results. At damage sizes of 40 mm and larger, the panels without imperfection have the lowest failure loads, and the geometrical imperfection seems to lower the sensitivity to damage for skin-stringer
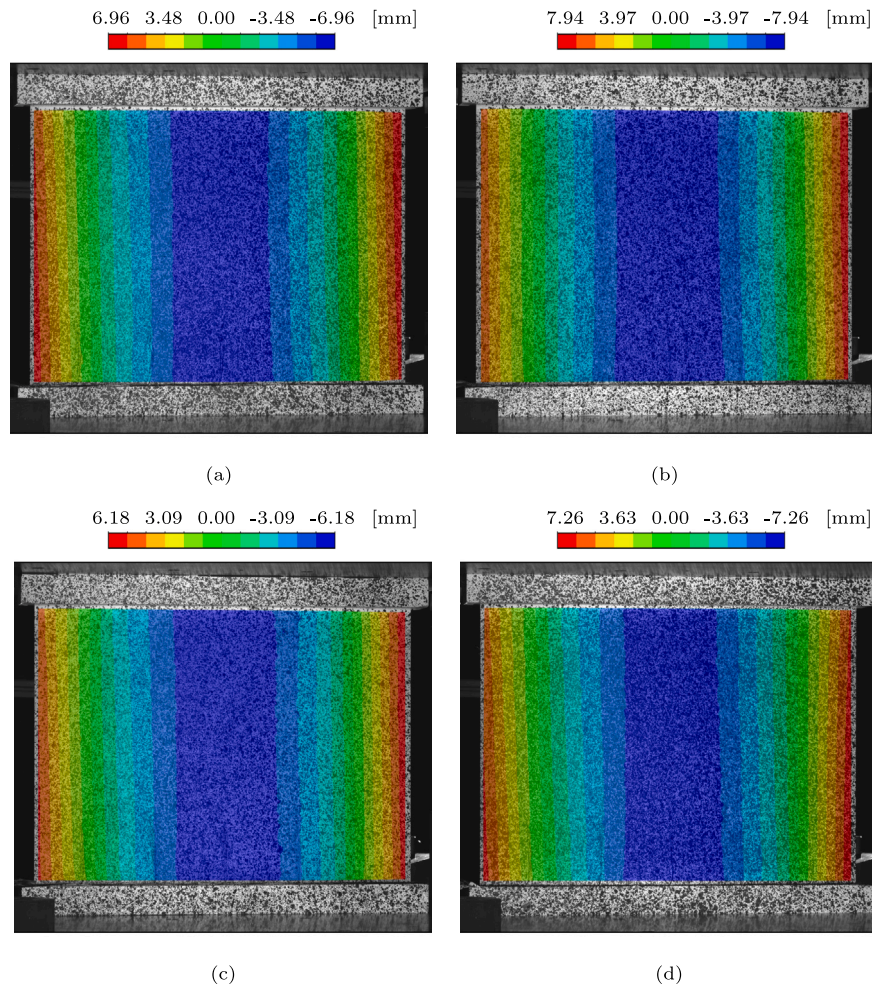
Fig. 12. Out-of-plane imperfection of test panels: (a) panel 1; (b) panel 2; (c) panel 3; (d) panel 4.

separation. At damage sizes of 55 mm and above, the lower bound for the failure load is between 230 and 250 kN, which is a reduction of 26%–32% of the failure load compared to a pristine panel.

The panels present the highest sensitivity to damage size between 25 mm and 55 mm, at a larger damage size the initiation and final failure load start to plateau. The explanation for this effect is twofold. Firstly, the initiation of skin-stringer separation seems to occur when the damage opens, of which the load does not seem to vary considerably above a certain damage size. Secondly, above a certain damage size, final failure occurs when the weld in the same stringer, but opposite flange of the damage location, becomes critical and separates in an unstable matter. This lowers the overall sensitivity to the damage size, as the opposite flange dominates final failure. The criticality of the opposite flange can be influenced by the opening of the damage, which is a rather stable increase of loading on the weld, but also due to buckling shape changes in the bay which can trigger sudden final failure.

Two damage sizes are investigated further to study the possible effect of imperfections on the buckling and failure behaviour of panels with damage in more detail.

The first investigation focuses on the damage size of 40 mm for different imperfection amplitudes of panel 2, as both the initiation load and failure load are highly affected. The load–displacement behaviour for the three imperfection amplitudes of 0, 0.5 and 1 is reported in Fig. 14(a). For no imperfection, a small load drop is seen at 230 kN, due to the opening of the initial damage and the start of separation, and final failure occurs at 244 kN. The imperfection amplitudes of 0.5 and 1 have a failure load of 328 and 276 kN, respectively, and experience no

load drop before final failure. Out-of-plane contour plots are reported in Fig. 14 (b–d), (e–g) and (h–j) for imperfection amplitudes 0, 0.5 and 1, respectively. The initial damage of 40 mm is on the left side of the panel. All three cases start initially with three half-wave buckling shapes with a clockwise skew regarding half-wave placement. At higher loads, a fourth half-wave appears in the bay with the initial damage for no imperfection, while the other two cases present no additional half-waves in the bays. For an imperfection amplitude of 0.5 the skew of the half-waves rotates anti-clockwise with increased load, and additional half-waves appear underneath the stringers.

The effect of the different buckling shapes, caused by different imperfections, on the skin-stringer separation behaviour and failure load is considerable. This seems to be related to the relative position of an outward half-wave w.r.t. to the initial damage, which can cause opening of the initial damage and start separation. The four half-wave buckling shape is most critical, where an outward half-wave with a shorter half-wave length is positioned close to the initial damage location. In this case separation starts at 230 kN, with a small load drop, followed by stable separation growth until a load of 244 kN. Then the middle stringer weld, opposite to the initial damage, starts to separate. The least critical case is with an imperfection amplitude of 0.5, where there is no outward half-wave close to the initial damage. At higher loads, the outward half-wave only moves further away, with the buckling shape having an anti-clockwise skew. Also, the curvature of the imperfection is highest in the weld region, which can also effect the separation behaviour.

The second investigation is on the damage size of 70 mm for different imperfection amplitudes of panel 1. The load–displacement
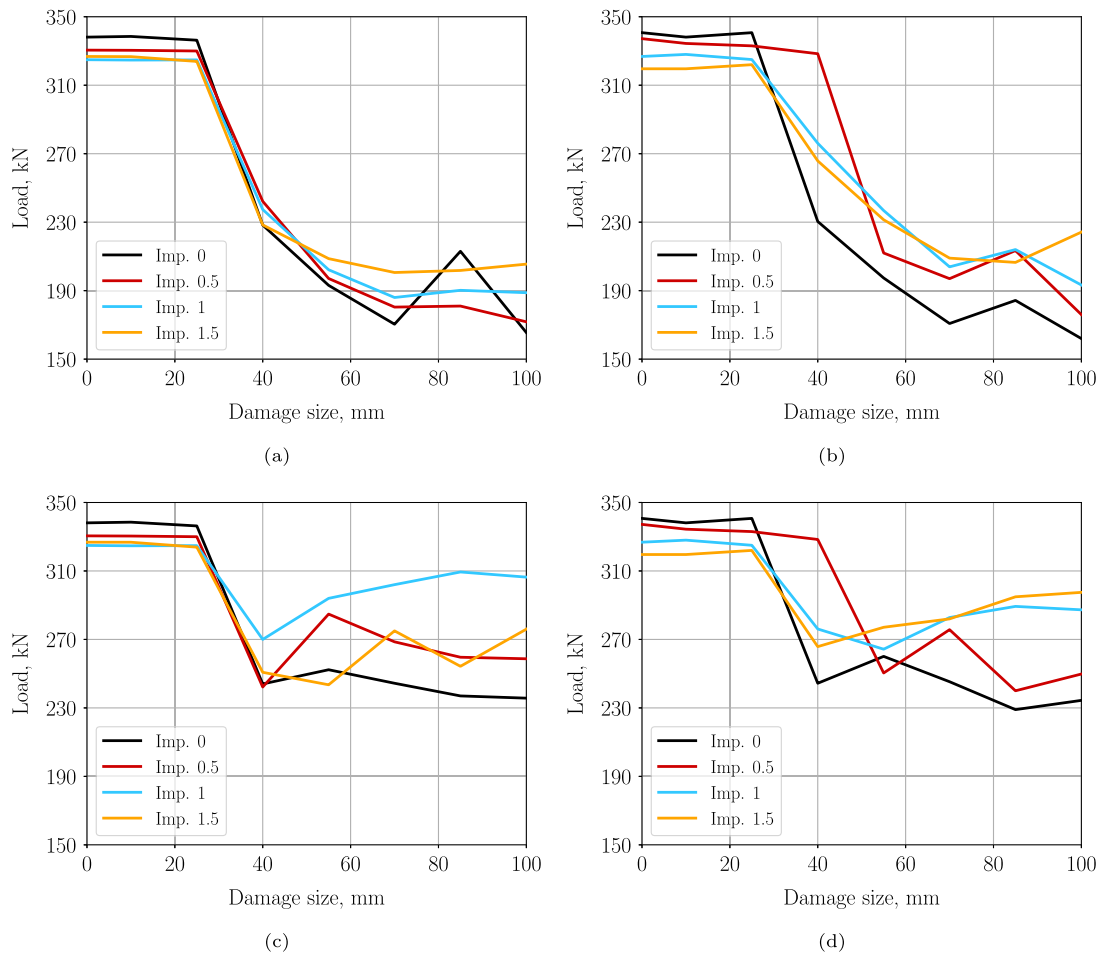
Fig. 13. Damage size sensitivity study results for different imperfection amplitudes: (a) initiation panel 1 imperfection; (b) initiation panel 2 imperfection; (c) final failure panel 1 imperfection ; (d) final failure panel 2 imperfection.

behaviour for the three imperfection amplitudes of 0, 0.5 and 1 is reported in Fig. 15(a), which present higher failure loads for a larger imperfection. After buckling, all three imperfection amplitudes experience a small load drop, which is caused by a small separation event at the initial damage location. Out-of-plane contour plots are reported in Fig. 15 (b–d), (e–g) and (h–j) for imperfection amplitudes 0, 0.5 and 1, respectively. For no imperfection, the initial buckling shape has three half-waves (b), and the initial damage opens shortly after a small load increase which results in an anti-symmetric buckling shape (c). The imperfection amplitudes of 0.5 and 1 present opening of the initial damage at the start of buckling (e–h), with an anti-symmetric buckling shape. All three amplitudes show stable separation growth of the initial damage after the first separation event, until final failure. The final failure of imperfection amplitudes 0 and 0.5 starts with the right bay switching buckling shape to four half-waves (d–g). This buckling shape change is not seen for an imperfection amplitude of 1.

At final failure, all three imperfection amplitudes show a similar amount of separation growth, with the separation length growing from 40 mm to approximately 162 mm. It is therefore difficult to judge how much the buckling shape change of imperfection amplitude 0 and 0.5 contributes to the start of final failure, and the separation length might be the main contributor. The imperfection amplitudes and resulting buckling shape differences do contribute to the differences in final failure, but indirectly by influencing the separation behaviour.

A larger imperfection delays the start of separation at 173, 183 and 192 kN for imperfection amplitude 0, 0.5 and 1, respectively. Also, for larger imperfections, this separation event caused less growth while occurring at higher loads. This can be considered counter-intuitive, as

one could expect that a higher load leads to more separation. This might be caused by the relatively high curvature of the imperfection in the weld region. The larger imperfection increases the curvature of the welded interface, which might increase the initiation and the failure load.

5.2. Damage location sensitivity

The initiation loads for single damage have a lower bound of approximately 230 kN, as reported in Fig. 16(a). For an offset of 0 mm, the initiation load is highly influenced by the imperfection amplitude, with the imperfection amplitude initially increasing the initiation load considerably and then converging to an intermediate load level between 230 and 270 kN. The results from different imperfection amplitudes converge for offsets between 44 and 110 mm, with the highest initiation load for no imperfection. The results diverge at offsets above 110 mm, with larger imperfections leading to higher initiation loads. This effect is caused by all cases between 44 and 110 mm offset presenting similar three half-wave buckling shapes, and more varying buckling shapes below 44 mm and above 110 mm offset. The higher sensitivity to the damage location between 44 and 110 mm offset is most likely caused by the relative location of the damage w.r.t. an outward buckling half-wave. The lower sensitivity at 132 mm for imperfection amplitudes 1 and 1.5 are caused by a buckling shape change underneath the stringers, and results at 154 mm offset are most likely starting to get affected by the proximity of the potting.

The final failure loads for single damage show less variance than the initiation loads, as reported in Fig. 16(c), with a lower bound of
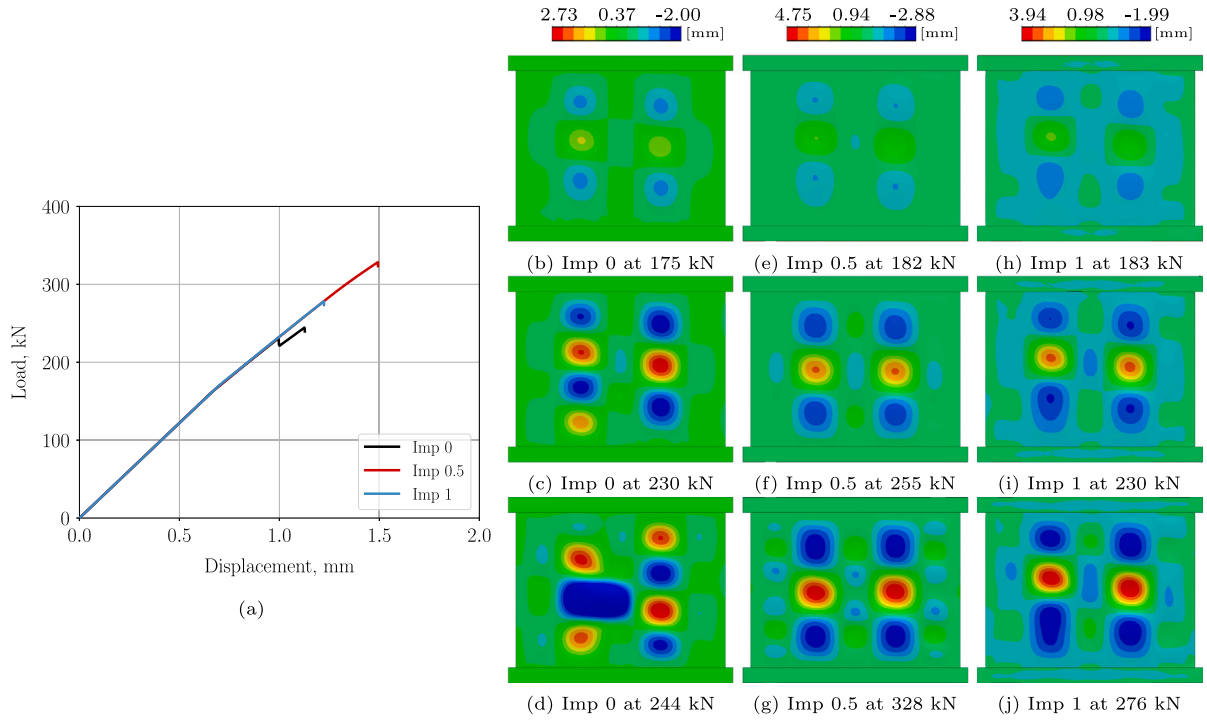
Fig. 14. Panels with 40 mm damage and panel 2 imperfection: (a) load–displacement; (b–g) out-of-plane displacement contour plots.
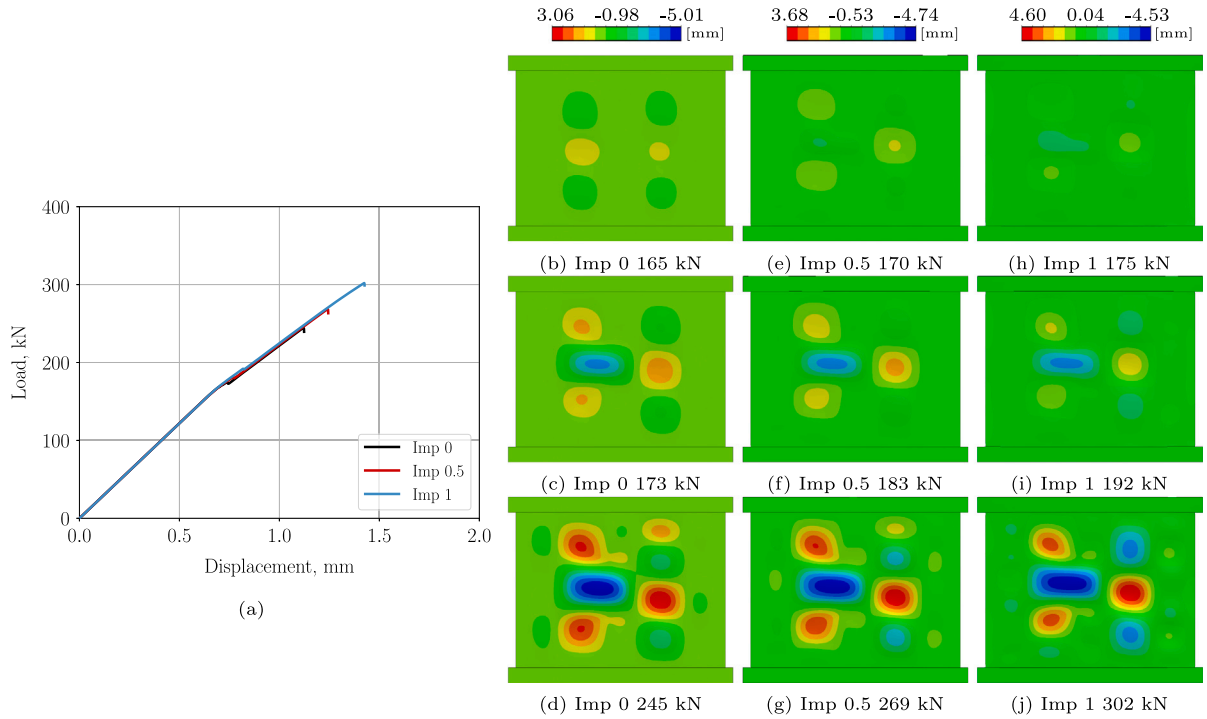

Fig. 15. Panels with 70 mm damage and panel 1 imperfection: (a) load-displacement; (b-g) out-of-plane displacement contour plots.

approximately 250 kN. The largest difference is seen at 0 mm offset, where the highest failure load is for the imperfection amplitude of 0.5. At high offsets of 132 mm and 154 mm, the imperfection amplitude of 1 and 1.5 shows the highest failure loads, where final failure occurs after the first initiation of skin-stringer separation. Most cases that present initiation above approximately 270 kN, collapse after initiation, while cases that experience initiation below 270 kN continue to carry load until approximately 270 kN.

The results of the sensitivity study with two initial damages shows initiation loads between 230 and 280 kN, as reported in Fig. 16(b). Imperfection amplitudes 1 and 1.5 result in similar behaviour over the whole offset range, while imperfection amplitudes 0 and 0.5 result in varying behaviour. There are three different ways in which initiation starts. Firstly, the damage at the middle of the panel starts, followed by the second damage. Secondly, the second damage with the offset starts, followed by the damage in the middle of the panel. Lastly, both damages experience initiation simultaneously. Offsets of 0 and
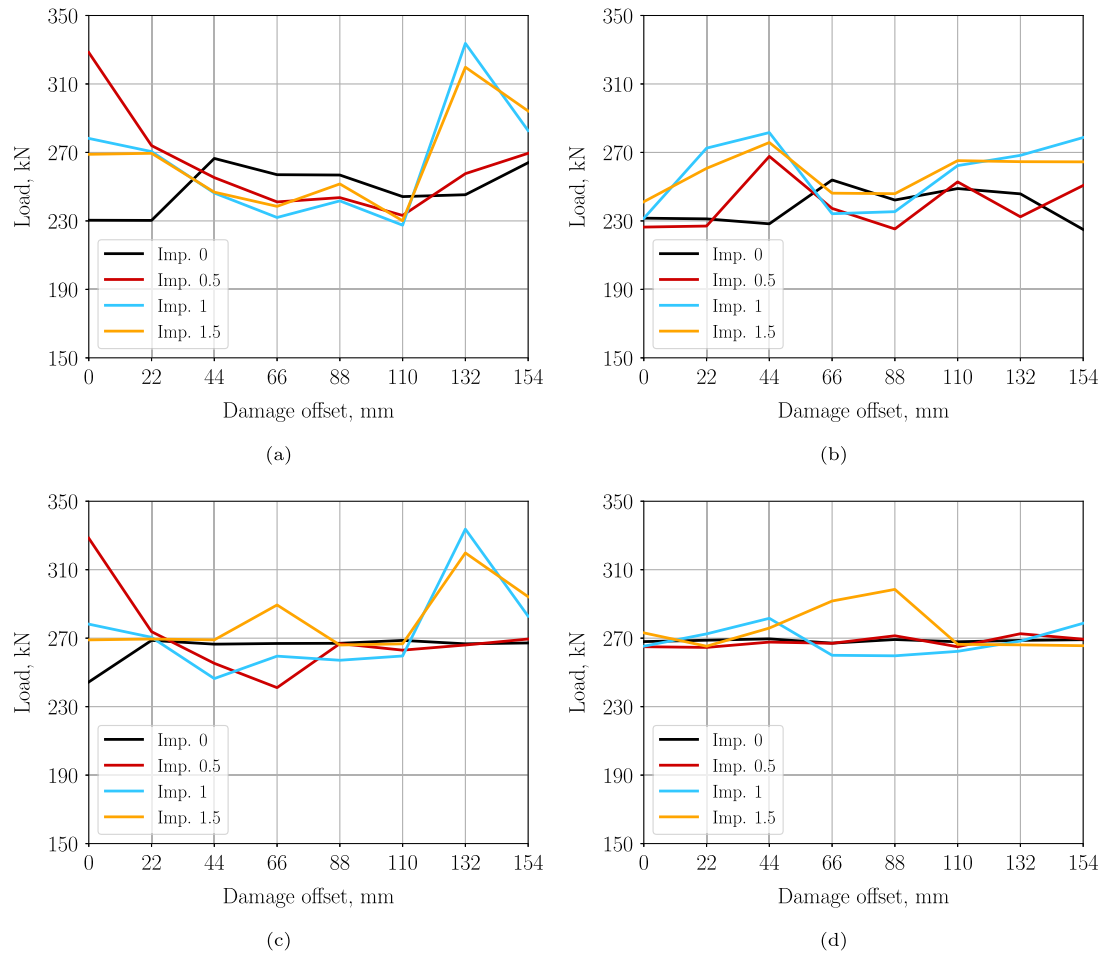
Fig. 16. Damage offset sensitivity study results with Panel 2 imperfection: (a) initiation damage 1; (b) initiation damage 2; (c) final failure damage 1 ; (d) final failure damage 2.
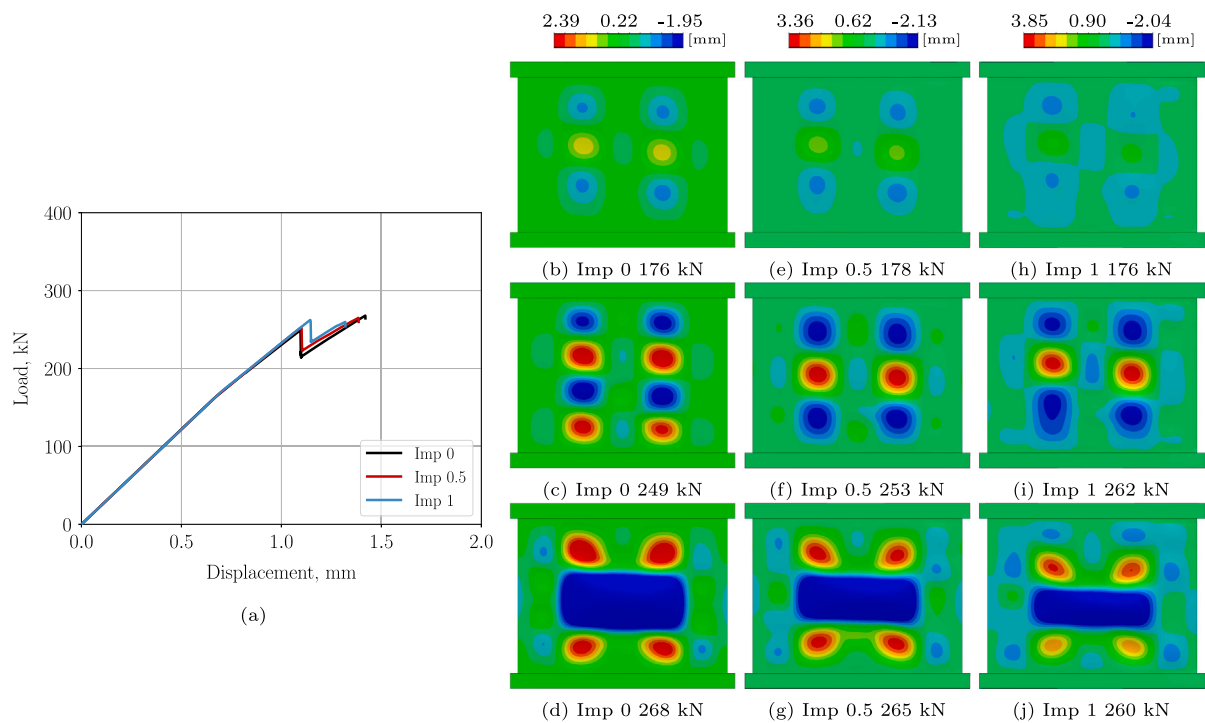

Fig. 17. Panels with two 40 mm damages with a 110mm offset, and panel 2 imperfection: (a) load-displacement; (b-g) out-of-plane displacement contour plots.

22 mm always experience simultaneous initiation, while 66 mm always initiates at the second damage. The remaining cases have varying behaviour, due to differences in buckling shapes and buckling shape evolution. One of the common factors seems the proximity of an outward half-wave, which increases the criticality of a damage location.

The failure load present little variation for the offset of the second damage, as reported in Fig. 16(d), with most failure loads at approximately 270 kN. Most cases show that after the initiation of the two damage locations, one tunnel (or one half-wave) is formed between the two locations, and final failure occurs after one of the side stringers exhibits skin-stringer separation. An exception is for an imperfection amplitude of 1.5 for an offset of 55 and 88 mm, which have a higher failure load, and there are two separate tunnels underneath the middle stringer.

The effect of the imperfection amplitude is investigated in more detail for an offset of 110 mm, as this offset is chosen for one of the test panels. The load–displacement behaviour for the three imperfection amplitudes of 0, 0.5 and 1 is reported in Fig. 17(a), which shows higher initiation load and a lower failure load for higher imperfection amplitudes. Out-of-plane contour plots are reported in Fig. 15 (b–d), (e–g) and (h–j) for imperfection amplitudes 0, 0.5 and 1, respectively. All three imperfection amplitudes start with a three half-wave buckling shape (b-e-h). The case of no imperfection presents a buckling shape change to four half-waves in both bays (c). The buckling shape evolution between imperfection amplitudes 0.5 and 1 shows differences in half-wave lengths and skew of the half-wave positions (f–i). After initiation, all three cases experience tunnelling behaviour underneath the middle stringer (d-g-j). For the case of no imperfection, initiation starts at the damage in the middle of the panel, while for the cases with an imperfection amplitude of 0.5 and 1, initiation starts at the second damage at an offset of 110 mm. After the initiation of skin-stringer separation, it presents a load-drop, followed by stable separation growth until final failure when one of the side-stringer starts to separate. The lower imperfection amplitudes have a lower initiation load, and more separation growth after the separation event, which seems to lead to a higher final failure load.

6. Test and numerical results

This section reports the test results of the panels, compares them to the numerical results, and focuses on the effect of each configuration.

6.1. Panel 1: pristine panel

The load, as measured by the load cell and the average of the LDS displacement measurement, is analysed. The load–displacement behaviour of the pristine panel is reported in Fig. 18. The panel has an approximate stiffness of 236 kN/mm, buckles at a load of 172 kN and fails at a load of 332 kN. At approximately 275 kN a small load drop is seen due to a sudden change in buckling shape. The numerical analysis is able to predict the overall structural behaviour well, but it does not predict the buckling shape change and resulting small load drop. This also leads to a larger difference in post-buckling stiffness, as the buckling shape change seen during the test also reduces stiffness.

The strains of the stringer cap are reported in Fig. 19(a). The loading imperfection is small, and in the post-buckling range, there is a small jump in strains which is caused by the sudden buckling shape change. The strains under the stringers are reported in Fig. 19(b). The strains underneath the stringer show equal loading and a drop in stiffness after buckling. The strains only diverge slightly and experience a sudden jump in strain due to a buckling-shape change.

The strains in bay 1 show a large jump due to the buckling-shape change, as reported in Fig. 19(c). This jump in strain is not seen in the numerical results, due to the lack of a buckling-shape change. The strains in bay 2, as reported in Fig. 19(d), show a higher bending component compared to bay 1, with a similar jump in strains due to
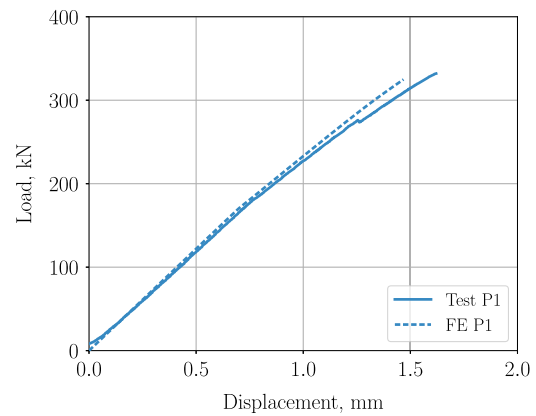

Fig. 18. Load–displacement curves from tests and numerical analysis of pristine panel.

the buckling shape change. The strains, as predicted by the numerical analysis, are very similar but lack the jump in strain due to buckling shape change.

The numerical analyses are able to predict the overall strains well but present differences in the post-buckling field, due to buckling-shape changes and skin-stringer separation events.

The post-buckling shape and evolution of the panels are determined from the DIC measurement and compared to the results from the numerical analysis. The displacement is positive for inwards direction and negative for outwards direction. The panel presents an initial three half-wave buckling shape until approximately 275 kN, after which a sudden buckling shape change occurs with a four half-wave buckling shape, as reported in Fig. 20. The numerical analysis predicts a three half-wave buckling shape. The number of half-waves underneath the stringer increases in the post-buckling field, similar to the test, but the buckling shape does not change.

The start of final failure is captured at 10000 fps by a highspeed camera. It starts with skin-stringer separation in the right flange of the middle stringer, which is followed by separation in the left flange of the middle stringer, as reported in Fig. 21(a–b). Before final failure occurs, small ticking sounds can be heard on the GoPro footage, indicating possible stable separation. The numerical analysis predicts the start of failure in the right stringer, as reported in Fig. 21(c–d). This difference can be caused by the differences in imperfection and buckling shape.

The post-failure state is reported in Fig. 22(a-b-c). All stringers have large separated areas, with more separation on the right-hand side of the panel. All stringers have fractures across the whole stringer width, and the flanges have large delaminations. The areas of the weld at the top of the panel have elliptical crack fronts.

6.2. Panel 2: one initial damage in middle stringer

The load–displacement behaviour of the panel with one initial damage in the middle stringer is reported in Fig. 23, in a comparison with the pristine panel. The panel has a stiffness of approximately 237 kN/mm and buckles at a load of 168 kN. Panel 2 fails due to skin-stringer separation at a load of 295 kN, while the pristine panel fails at a load of 332 kN. This is a reduction of the failure load of 11.2% due to the damage in the flange of the middle stringer. The numerical analysis of panel 2 is able to predict the overall structural behaviour well. The biggest difference is seen for the failure load, which is conservative with a 6.4% lower failure load compared to the test.

The strains on the cap of the panel are reported in Fig. 24(a), where it is seen that S9 shows lower strains compared to S1 and S5. A small loading imperfection can cause this difference. The strains under the stringers are equal, and there is no sign of unequal loading
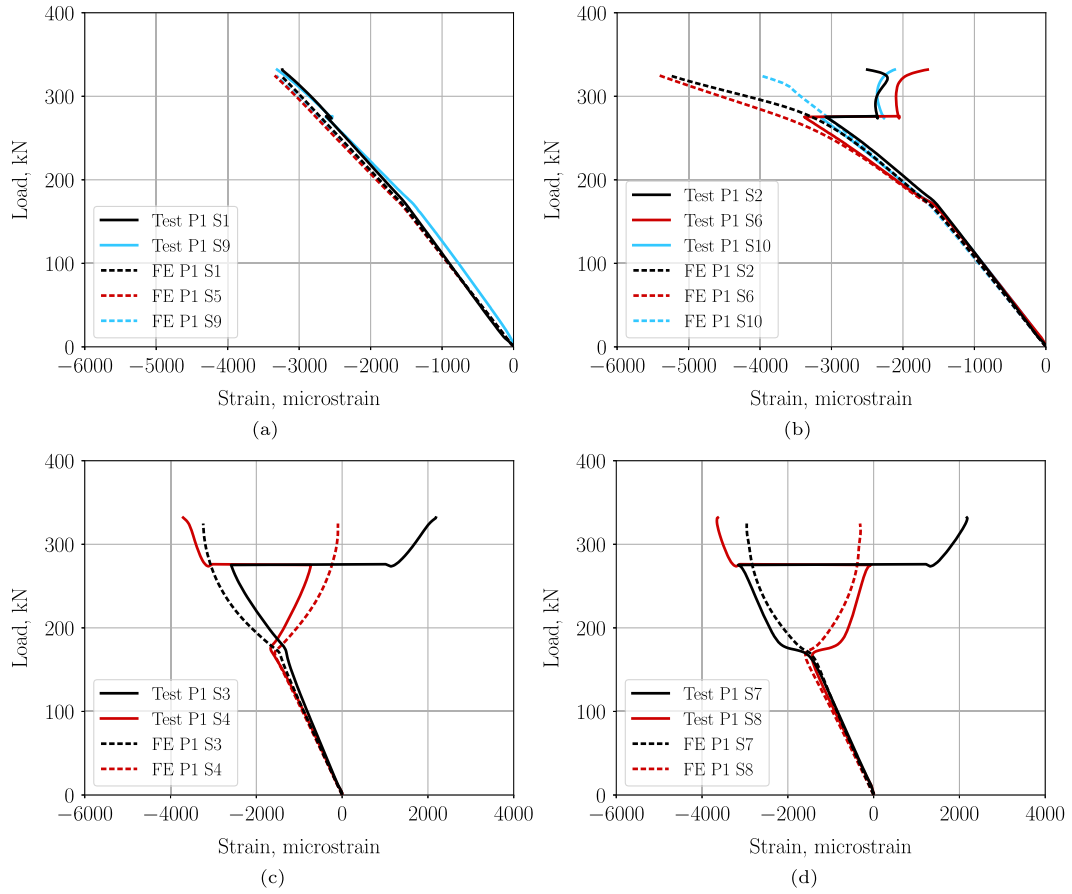
Fig. 19. Experimental and numerical compressive strains of the pristine panel: (a) caps; (b) skin under stringer; (c) bay 1; (d) bay 2.
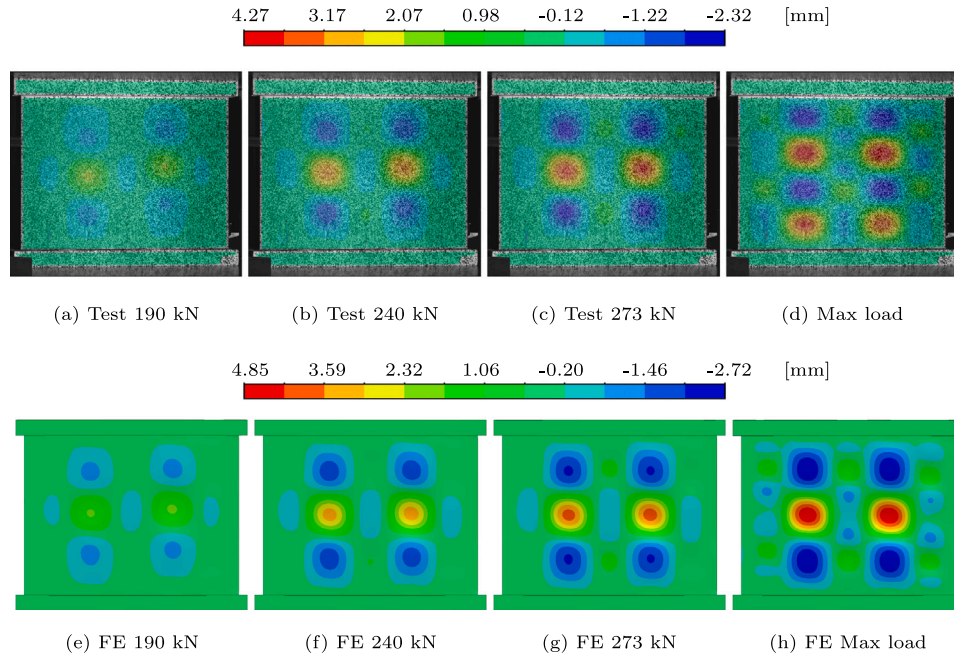

Fig. 20. Experimental (a–d) and numerical (e–h) out-of-plane displacement of the pristine panel.

of the skin Fig. 24(b). A slight drop in stiffness can be seen initially when buckling occurs after which the strains diverge, probably due to the different half-wave positions underneath each stringer, with more divergent behaviour close to the failure load.

The strains in bay 1 present slight divergent behaviour initially after buckling, as reported in Fig. 24(c). When the buckling-shape further develops, the strains diverge more and experience a large bending component. The numerical prediction shows less divergent strains and
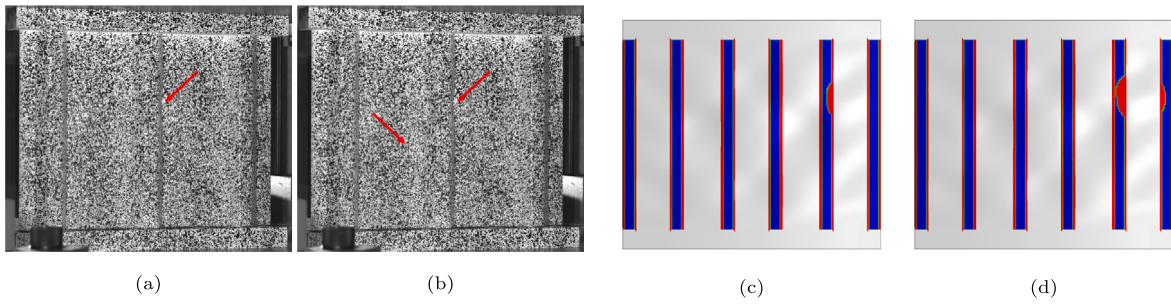
Fig. 21. Comparison of failure behaviour of pristine panel: (a) start of failure during test; (b) propagation of failure during test; (c) start of failure in analysis; (d) propagation of failure in analysis.
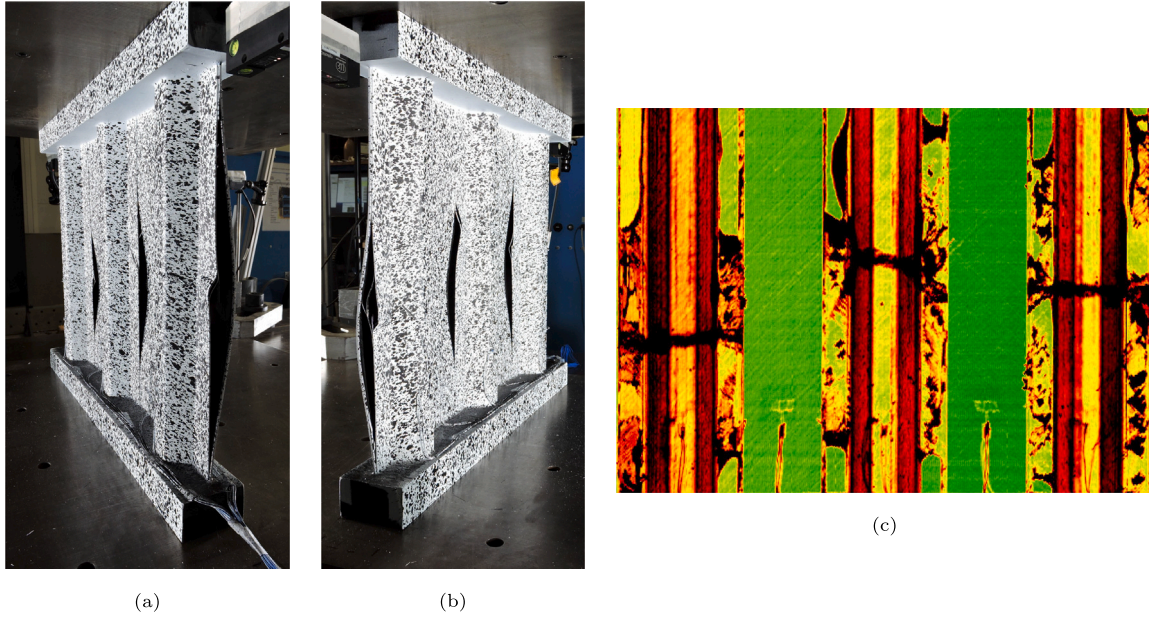

Fig. 22. Post-failure of pristine panel: (a) photo from right side; (b) photo from left side; (c) c-scan.
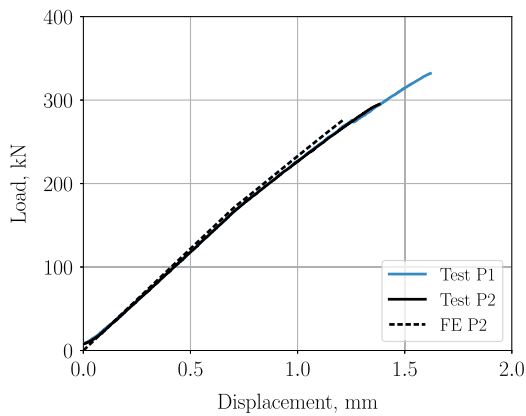

Fig. 23. Load–displacement curves from tests and numerical analysis of panel 2.

in opposite direction, due to differences in buckling shape. The strains in bay 2 are reported in Fig. 24(d). There is comparable behaviour to the strains in bay one, with slightly more divergent behaviour. The numerical prediction, however, predicts almost linear strains, with only a small bending component which switches sign several times.

The panel shows an initial three half-wave buckling shape, with the half-waves positioned towards the top of the panel, as reported

in Fig. 25. The buckling shape evolves to a four half-wave buckling shape, and just before final failure, the outwards half-waves in the bay and underneath the stringer start to connect. The numerical analysis predicts a three half-wave buckling shape, which evolves in terms of out-of-plane displacement magnitude and half-wave length. The difference in buckling shape compared to the test can be due to the differences in geometrical imperfection and loading imperfection.

The start of failure is reported in Fig. 26(a), which is captured by a high-speed camera at 10000 fps. Separation starts in the right flange of the middle stringer, at the initial damage location. This is followed by separation of the left flange, as reported in Fig. 26(b), and then the stringer further separates in upwards and downward directions. The numerical analysis also predicts this behaviour, as reported in Fig. 26(c-d). There is an elliptical crack front shape for the separation at the initial damaged location and in the opposing flange.

The post-failure state of panel 2 is reported in Fig. 27(a–b). It is seen that both the left and middle stringer have large separations. The left stringer has a larger separated area compared to the middle stringer, while the middle stringer had initial damage in the right flange. Final failure started with separation at the damaged location, which caused further large separations in the left-hand side of the panel. The right stringer's interface has some small separated areas, and the weld presents small elliptical fronts. The right flange of the left stringer shows material damage, with a fracture that starts from the lower radius to the flange edge.
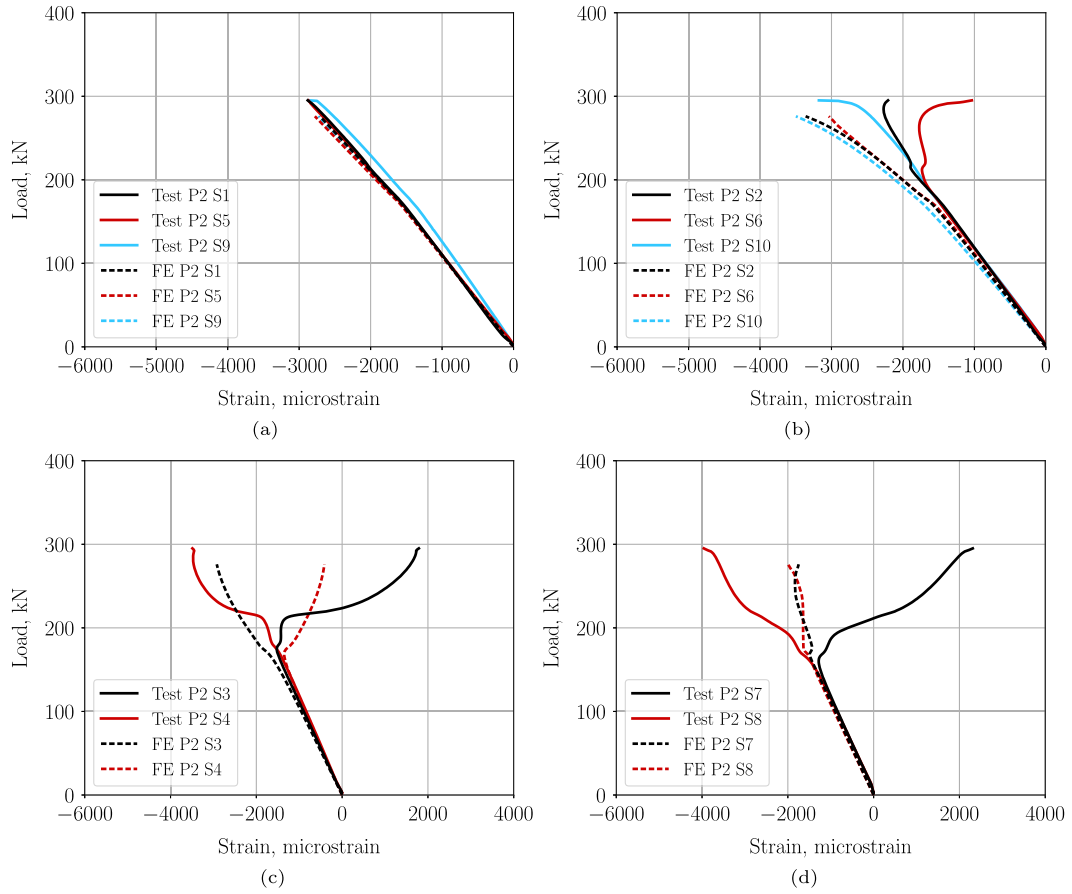
Fig. 24. Experimental and numerical compressive strains of the panel 2: (a) caps; (b) skin under stringer; (c) bay 1; (d) bay 2.
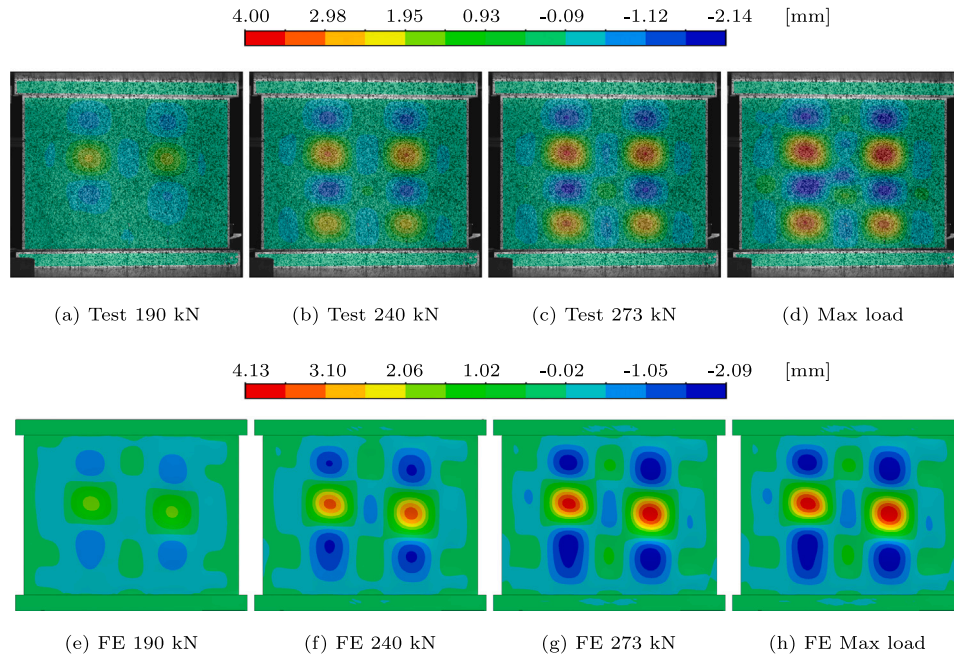

Fig. 25. Experimental (a–d) and numerical (e–h) out-of-plane displacement of panel 2.

6.3. Panel 3: two initial damages in middle stringer

The load–displacement behaviour of panel 3 is reported in Fig. 28. Panel 3 has a stiffness of approximately 236 kN/mm, and it buckles at a load of 173 kN. The panel experiences a maximum load of 277 kN at 1.29 mm of displacement, after which a load drop occurs. The panel fails at a load of 270 kN and 1.48 mm of displacement. This maximum load is 16.6% lower compared to the pristine panel. The
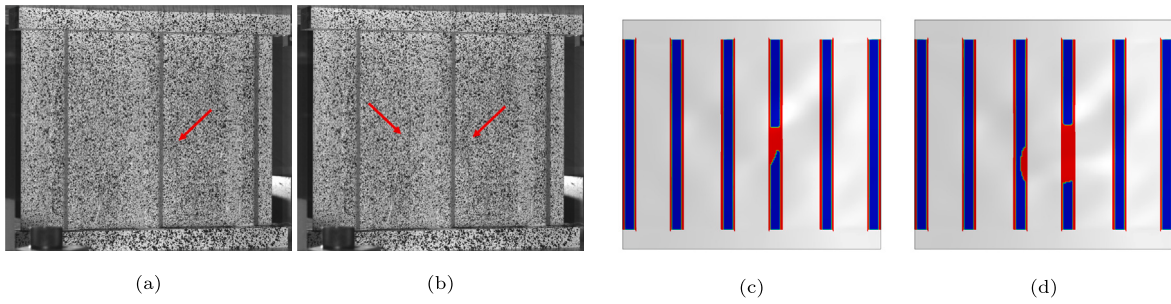
Fig. 26. Comparison of failure behaviour of panel 2: (a) start of failure during test; (b) propagation of failure during test; (c) start of failure in analysis; (d) propagation of failure in analysis.
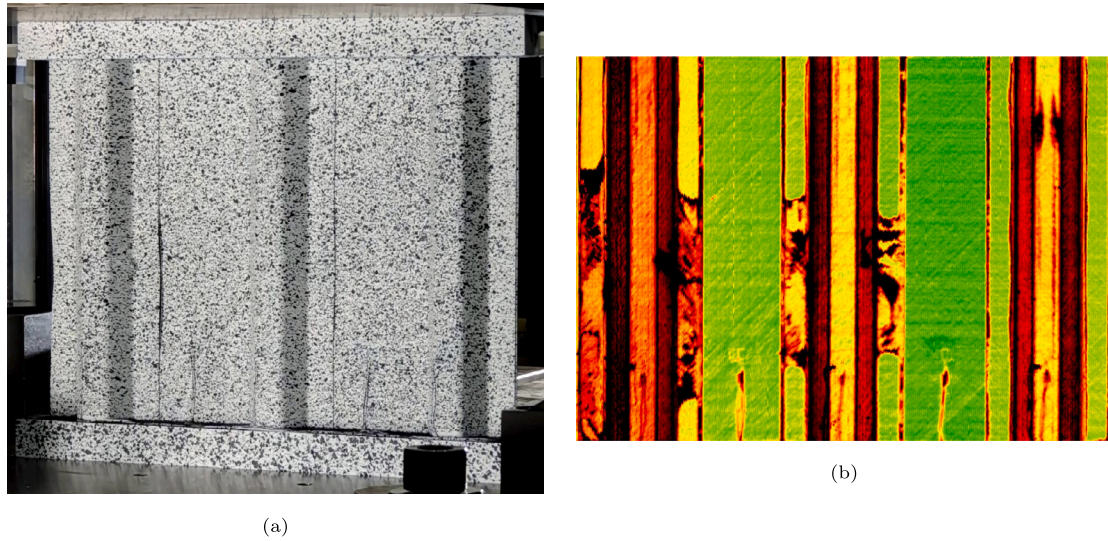

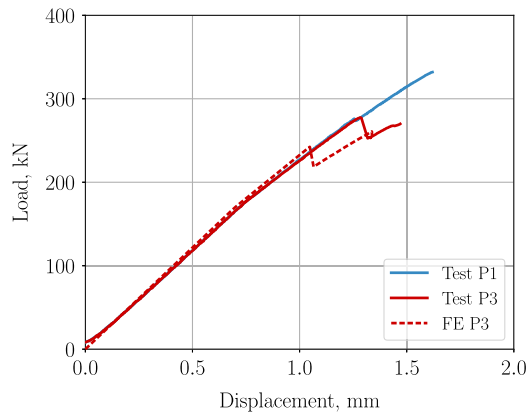**Fig. 27.** Post-failure of panel 2: (a) photo; (b) c-scan.

Fig. 28. Load–displacement curves from tests and numerical analysis of panel 3.

numerical analysis predicts similar behaviour with a load drop due to a skin-stringer separation event before final failure. It is, however, seen that this load-drop occurs at an 11.9% lower load, and the maximum load is 5.8% lower compared to the test.

The strains on the caps of the panels are reported in Fig. 29(a). It is seen that there might be a small loading imperfection, and a load drop due to a skin-stringer separation event. The strains underneath the stringer are reported in Fig. 29(b). Before buckling a minor difference in strains can be seen in the skin, indicating a small loading imperfection. After buckling the strains diverge, with large strain changes in the

post-buckling field. These large changes are caused by the skin-stringer separation event, which also leads to a load drop.

The strains in bay 1 start to diverge immediately after buckling, and show jumps in strain due to the skin-stringer separation event, as reported in Fig. 29(c). The numerical analysis predicts similar behaviour initially, although with opposite bending component, and larger jumps in strain in the post-buckling field. The strains in bay 2 present a high bending component in the post-buckling field, as reported in Fig. 29(d). A strain jump occurs due to the skin-stringer separation event, with S7 also presenting an increase in strains just before the separation event. The numerical analysis predicts an opposite bending component with larger jumps of strain in the post-buckling field due to the skin-stringer separation event.

Panel 3 shows a four half-wave initial buckling shape, with the fourth half-wave barely visible in bay two, as reported in Fig. 30. At higher load levels the fourth half-waves become more prominent. At 277 kN the initial damage opens, with the outward half-waves in the bay and underneath the stringer connecting. After the skin-stringer separation event there is large out-of-plane displacement in the middle of the panel, due to the separation between skin and stringer. At 270 kN, just before final failure, the large half-wave in the middle of the panel grows towards the side of the panel. The numerical analysis predicts a three half-wave buckling shape, with an anti-clock-wise skew in terms of half-wave position. At 218 kN, after the skin-stringer separation event, a large area of high out-of-plane displacement is seen, similar to the test results. At 263 kN the area of high out-of-plane displacement has moved upwards, indicating separation growth in an upwards direction.
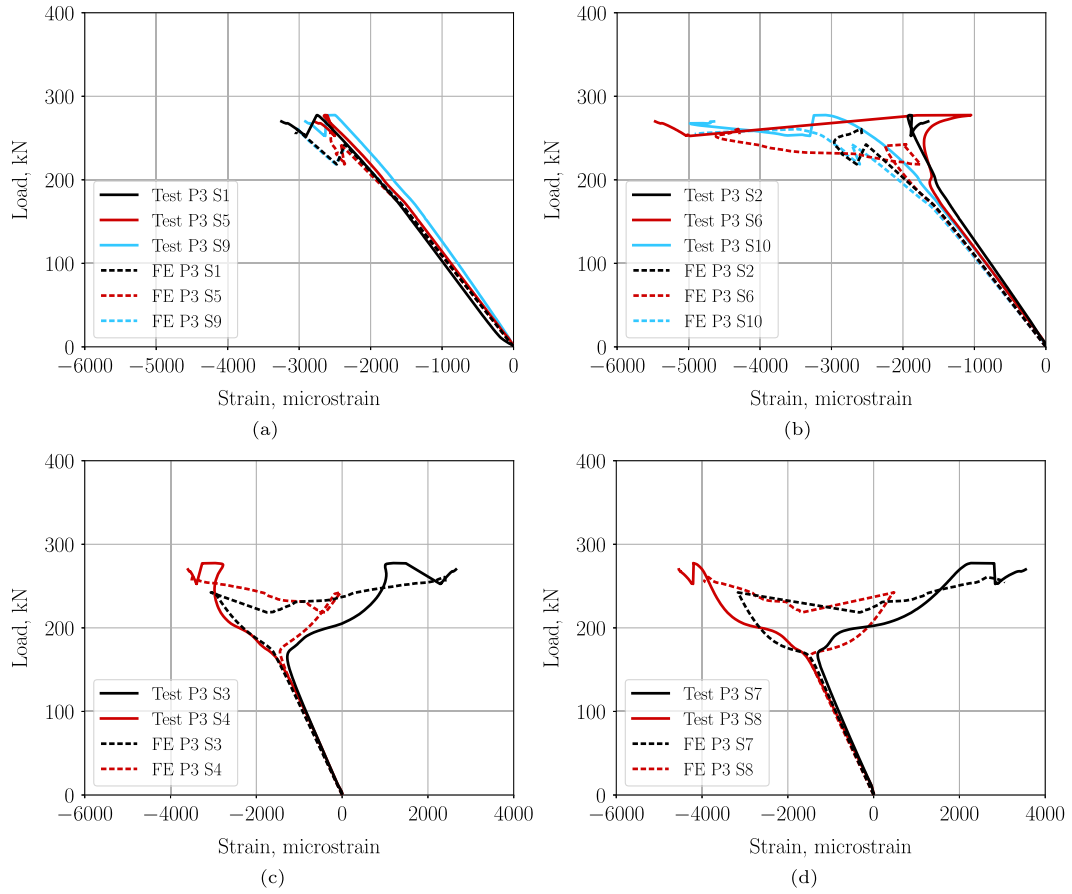
Fig. 29. Experimental and numerical compressive strains of the panel 3: (a) caps; (b) skin under stringer; (c) bay 1; (d) bay 2.

(a) Test 190 kN   (b) Test 240 kN   (c) Test 277 kN   (d) Test 253 kN   (e) Test 270 kN

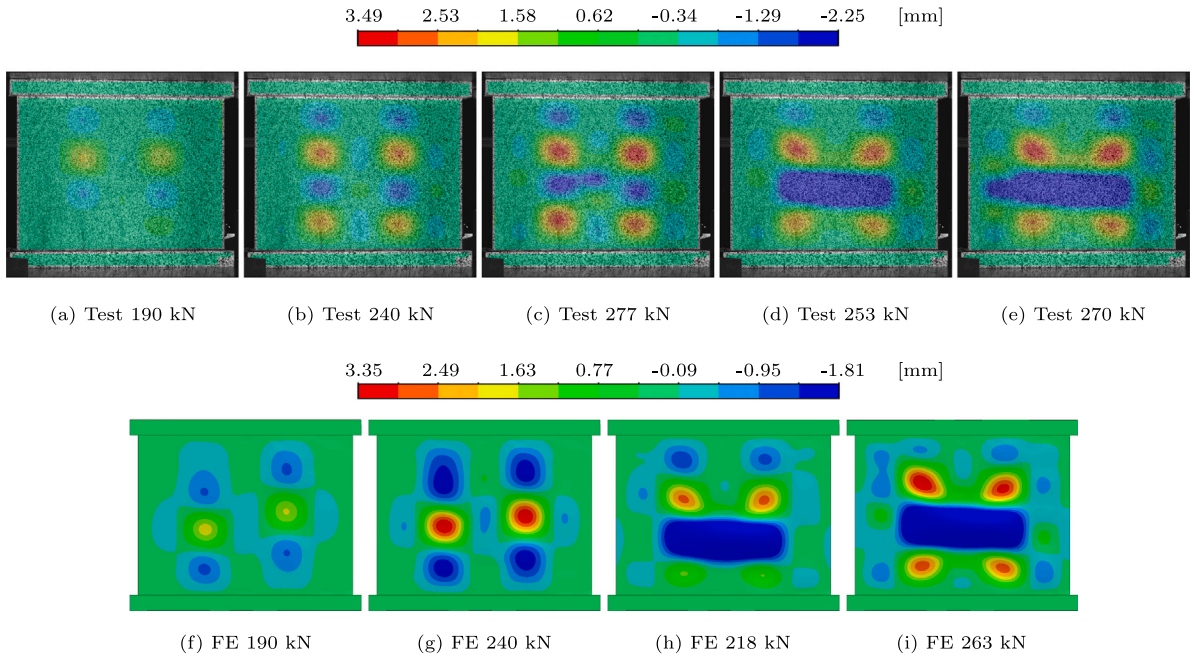(f) FE 190 kN   (g) FE 240 kN   (h) FE 218 kN   (i) FE 263 kN

Fig. 30. Experimental (a–e) and numerical (f–i) out-of-plane displacement of panel 3.

Panel 3 endured a skin-stringer separation event of the middle stringer, which did not lead to panel collapse, as reported in Fig. 31(a). The event started with stable crack growth, heard on the GoPro camera footage, for approximately 15 s. This stable crack growth seems to occur at the initial damage in the middle of the panel, as DIC measured an increase in out-of-plane displacement at this location. The stable crack growth is followed by unstable crack growth that results in a large separated area. After loading continued, final failure occurred
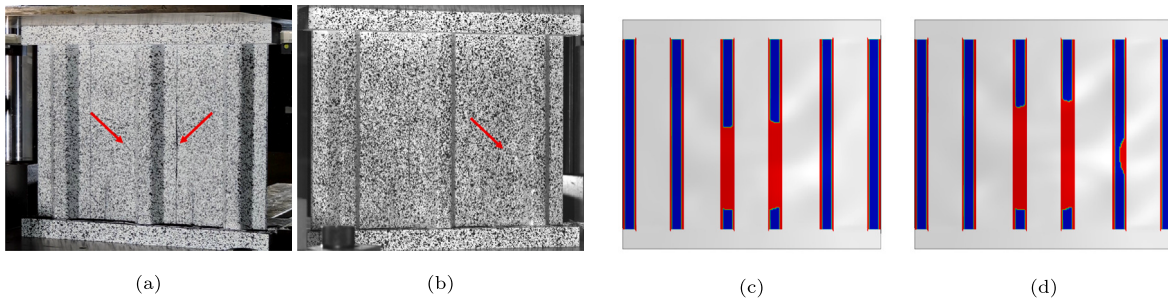
Fig. 31. Comparison of failure behaviour of panel 3: (a) start of failure during test; (b) propagation of failure during test; (c) start of failure in analysis; (d) propagation of failure in analysis.
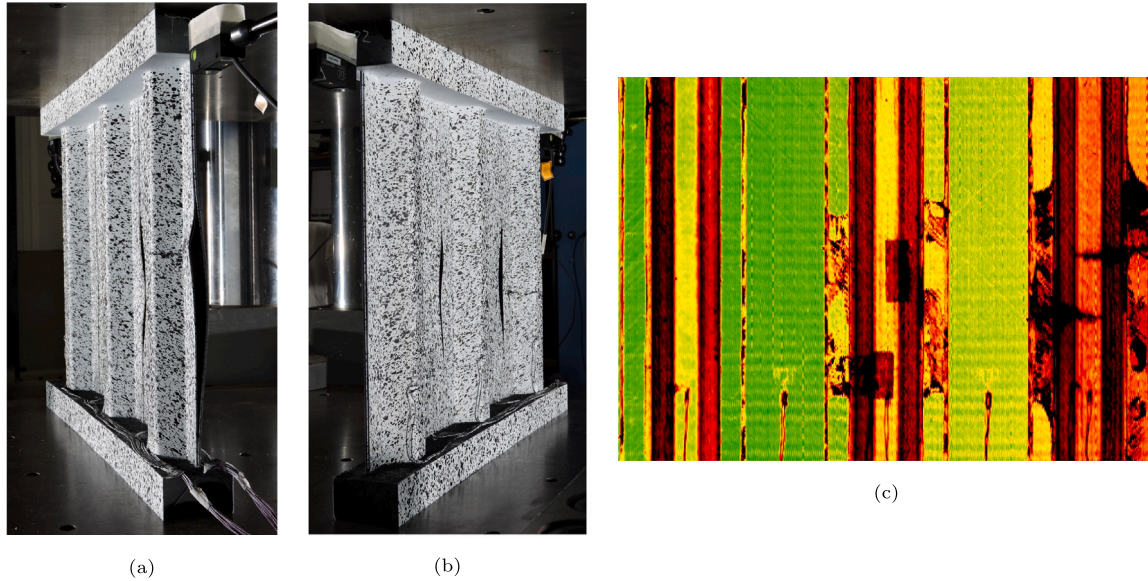

Fig. 32. Post-failure of panel 3: (a) photo right side; (b) photo left side; (c) c-scan.

with further separation of the middle stringer, followed by separation of the right stringer, as reported in Fig. 31(b). Similar behaviour is predicted by the numerical analysis, as reported in Fig. 31(c-d). Both flanges of the middle stringer separate initially, and final failure starts by separation of the right stringer.

The post-failure state of panel 3 is reported in Fig. 32(a-b-c). The middle and right stringer present large separated areas, with the right stringer having the largest separated area. The right stringer also presents two fractures across the stringer, in the middle of the panel. All flanges which have separated also have delaminations of the stringer flanges. The left stringer has no visible separations and no material damage.

After the test, the middle stringer of panel 3 is removed to investigate the fracture surfaces of the failed welds. The weld can be distinguished by the rough surface with visible fibres Fig. 33(b). The area in between the red dashes corresponds to the area that separated during the test. The two yellow foils of the initial damage are visible on the skin, while on the stringer two smooth areas can be seen that correspond to the same initial damage locations. The areas in between the purple and green dashes are highlighted in Fig. 33(a) and (c), respectively. The skin is mostly intact in the area that separated in the test, with limited fibre pullout and no obvious delaminations. The stringer has a few locations with delaminations, and small pieces of the stringer ply remain on the skin. The bottom 0 ply of the stringer is visible in a few small areas where the bottom 45 ply has delaminated.

On the fracture surfaces, lighter and darker areas can be identified. There are lighter areas around the middle initial damage and the

opposite weld, with an elliptical shape. These areas correspond to the location where DIC measured higher out-of-plane displacement before the first separation event. This might indicate that the lighter areas are caused by stable crack growth, while the darker areas are due to unstable crack growth.

On the fracture surface on the opposite side of the middle initial damage, next to the elliptical lighter area associated with the stable crack growth, dark elliptical marks can be seen. These markings indicate crack growth with an elliptical crack front shape. The crack growth seems to go in a sideways direction towards the bay and a downward direction towards the second initial damage location.

6.4. Panel 4: one damage in side stringer

The load–displacement behaviour of panel 4 is reported in Fig. 34. Panel 4 has an approximate stiffness of 236 kN/mm before buckling. It buckles at a load of 177 kN and fails at a load of 284 kN. This is a reduction of 14.5% in comparison to the pristine panel failure load. The numerical analysis over-predicts the failure load by 9.3%, which is the largest difference between numerical results and test results of all panels. This might be due to the location of the damage, which is in one of the side stringers.

The strains of the stringer caps are reported in Fig. 35(a). They are comparable to the previous panels, with a small reduction in strains of S9 just before final failure. The strains under the stringers are reported in Fig. 35(b). In post-buckling they present jumps and divergent
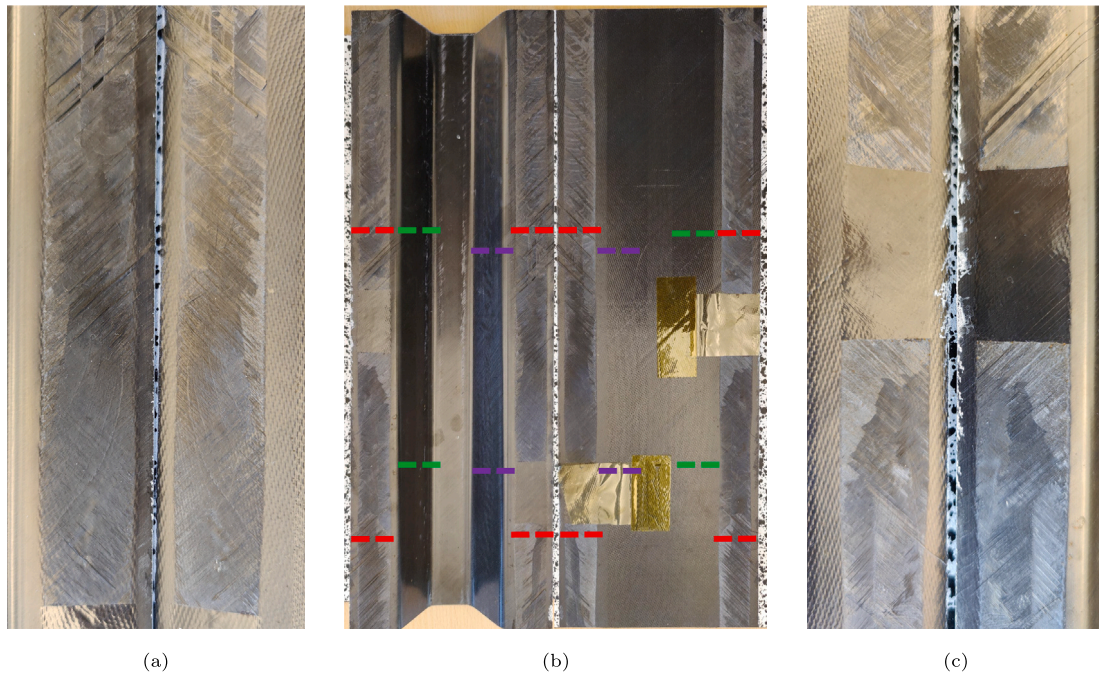
(a)

(b)

(c)

Fig. 33. Fracture surface of welds of middle stringer of panel 3; (a) close-up of the area between purple dashes; (b) fracture surfaces of middle stringer, with the stringer and skin on the left and right side respectively, with red dashes indicating the area that separated in the test; (c) close-up of the area between green dashes.
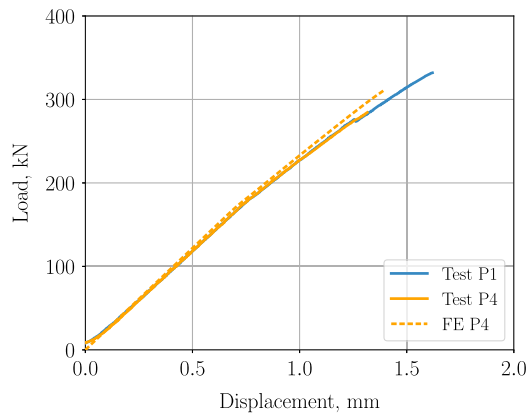

Fig. 34. Load–displacement curves from tests and numerical analysis of panel 4.

behaviour due to buckling shape changes, and a sudden increase just before final failure.

The strains in bay 1 show convergent behaviour initially after buckling, as reported in Fig. 35(c). Then they suddenly diverge considerably with a large bending component. The numerical analysis predicts diverging strains immediately after buckling, with a jump in the post-buckling field. The strains in bay 2 present similar behaviour to bay 1, as reported in Fig. 35(d). In post-buckling, they present an initial small bending component, after which the strains diverge due to high bending levels. The numerical analysis predicts divergent strains at a lower load, indicating buckling in the bay starts at a lower load than the test.

The panel has an initial three half-wave buckling shape, with the half-waves positioned towards the top of the panel, as reported in Fig. 36. The bottom inwards half-waves have a higher half-wave length, and at higher loads the fourth half-waves appear at this position. At the maximum load the damage in the stringer opens, with inward half-waves connecting between the bay and underneath the stringer. The numerical analysis predicts a three half-wave buckling shape, with the

half-waves initially positioned towards the bottom of the panel. At higher load levels, the half-waves evolve towards the top of the panel, and the number of half-waves underneath the stringer increases.

The final failure is captured by the high-speed camera and starts in the left flange of the right stringer, where the initial damage is located, as reported in Fig. 37(a). This is followed by the separation of the right flange of the same stringer, Fig. 37(b). Before final failure occurs, a ticking sound can be heard on the GoPro footage, indicating stable separation. The numerical analysis predicts the same start location at the initial damage, Fig. 37(c). Then separation starts in the right flange of the right stringer and in the middle stringer's left flange, as reported in Fig. 37(d). This behaviour was not seen during the test.

The post-failure state of panel 4 is reported in Fig. 38(a-b). Only the right stringer has large separated areas, with a fracture in the right flange. The middle stringer welds present small separations at the inner weld edge, as the weld becomes slightly narrower in some areas.

7. Summary and discussion

The pre-buckling stiffness, buckling load and maximum loads of the four tests and numerical analyses are reported in Table 6. The panels show a similar stiffness of approximately 236 kN/mm. The numerical analysis overpredicts the linear stiffness by 3.1% on average, and the post-buckling stiffness is overestimated similarly. This can be attributed to the assumed material properties or differences in laminate thickness. The buckling load varies slightly between the panels, which can be caused by differences in initial damage and imperfections. The numerical analysis predicts the buckling load accurately, with a maximum difference of 2.8%.

The failure load is highly affected by the initial damage, with one and two damages of 40 mm in the middle stringer decreasing the failure load by 11.2% and 16.6%, respectively, compared to the pristine panel. The damage in the side stringer decreases the failure load by 14.5%. The numerical analyses predict all failure loads within 10%, with the largest differences for panel 4, with an overprediction of 9.3%. The failure loads of the other three panels are predicted conservatively, with a maximum difference of 6.4%.
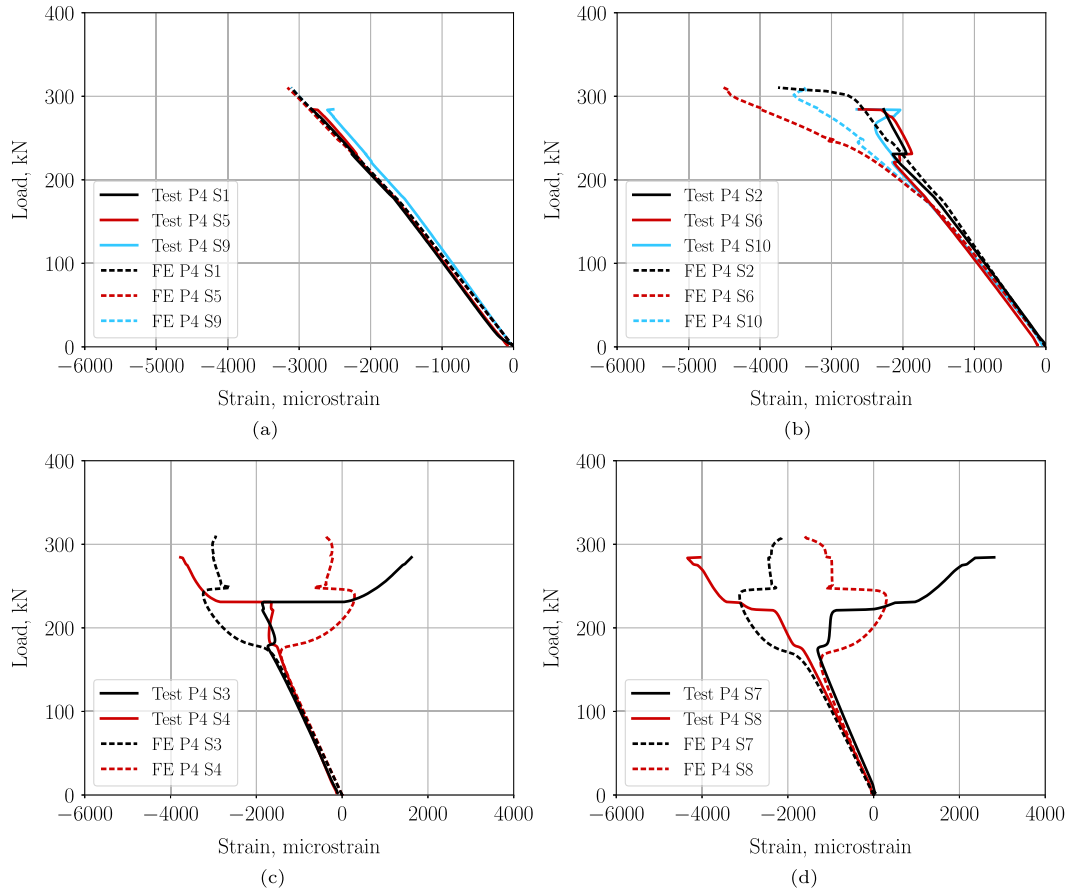
Fig. 35. Experimental and numerical compressive strains of the panel 4: (a) caps; (b) skin under stringer; (c) bay 1; (d) bay 2.
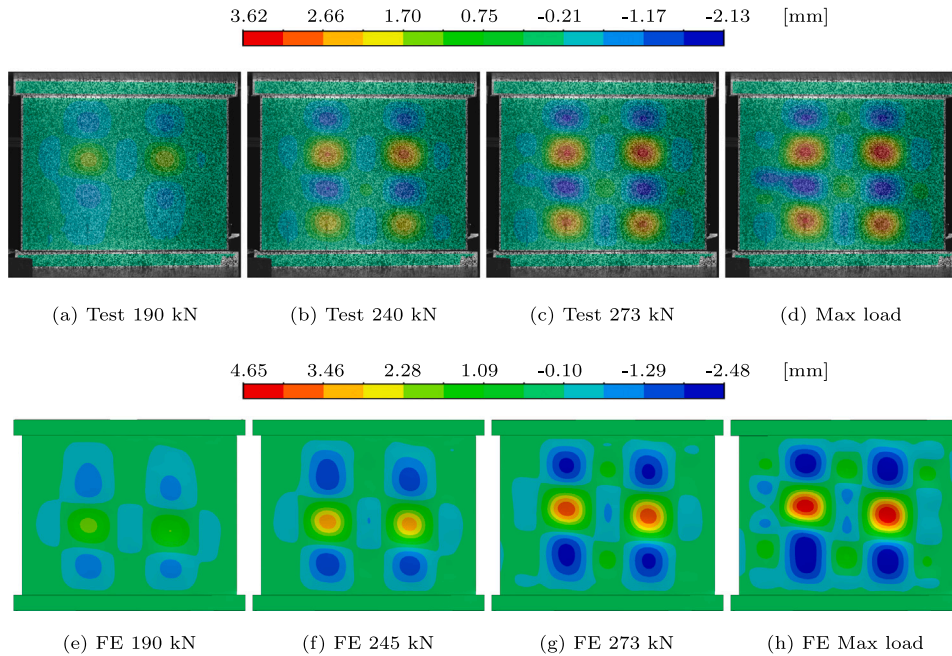

Fig. 36. Experimental (a–d) and numerical (e–h) out-of-plane displacement of panel 4.

The post-buckling strains underneath the stringer and in the bays are highly affected by the buckling shape (Figs. 19, 24, 29 and 35), which in turn can be affected by the location of the initial damage. Each damaged configuration shows different behaviour due to the different damage locations, and the numerical prediction has difficulty predicting the exact buckling shape.

All panels show a four half-wave buckling shape in the test. The fourth half-wave appears gradually for all damaged configurations
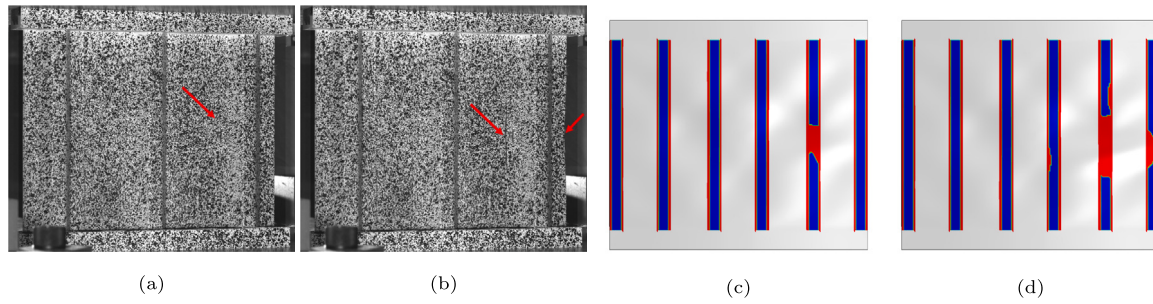
Fig. 37. Comparison of failure behaviour of panel 4: (a) start of failure during test; (b) propagation of failure during test; (c) start of failure in analysis; (d) propagation of failure in analysis.
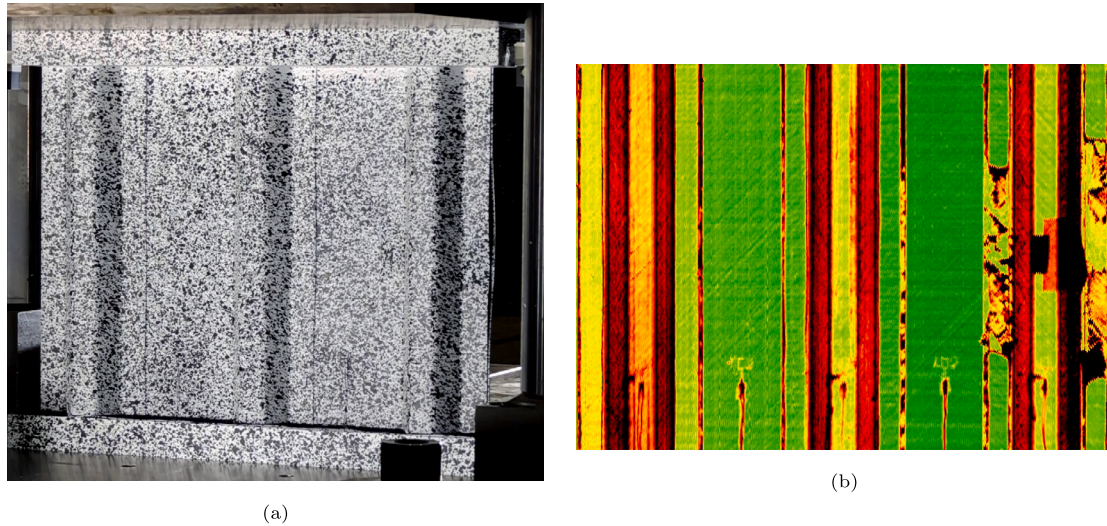

Fig. 38. Post-failure of panel 4: (a) photo; (b) c-scan.

Table 6
Pre-buckling stiffness, buckling load and maximum load from tests and numerical analysis.

	Pre-buckling stiffness			Buckling load			Maximum load		
	Test [kN/mm]	FE [kN/mm]	Diff. [%]	Test [kN]	FE [kN]	Diff. [%]	Test [kN]	FE [kN]	Diff. [%]
Panel 1	236.4	243.9	3.2	172	170	1.2	332	325	2.1
Panel 2	236.8	243.7	2.9	168	170	1.2	295	276	6.4
Panel 3	236.4	243.5	3.0	173	171	1.2	277	261	5.8
Panel 4	236.4	243.8	3.1	177	172	2.8	284	310	9.3

(Figs. 25, 30 and 36), while the pristine panel endured a sudden jump from three to four half-waves (Fig. 20). The initial damage locations appear to "attract" the half-waves and the opening of the initial damage can be seen from the DIC measurement. The opening seems to grow, indicating that stable separation occurs followed by unstable skin-stringer separation. Indications of stable separation can be heard from the GoPro footage of all panels with initial damage, and most notable on the footage of panel 3. The fracture surface of panel 3 also showed lighter areas around the damage location, indicating stable separation growth (Fig. 33). It is however difficult to determine how much separation growth occurs before final failure, without utilizing other measurement techniques more specifically for capturing damage growth.

The numerical analysis has difficulty predicting the influence of the initial damage on the buckling shape (Figs. 20, 25, 30 and 36). Instead of predicting four half-waves, the three half-wave buckling shapes show longer half-wave lengths, for the outwards half-waves close to the locations with initial damage. These structures are highly sensitive to imperfections, and the difference between test and analysis might be caused by how, and which imperfections are included in the

analysis. The geometrical imperfections, introduced in the analysis, are measured from the skin-side. Also, the initial damage is modelled as a perfect sharp crack, and no foil is simulated, which can influence the effect of the initial damage on the weld.

All panels fail due to skin-stringer separation. Panel 3, with two initial damages, showed a skin-stringer separation event of the middle stringer, where both welds separated approximately from the bottom to the top damage (Fig. 31). This, however, did not lead to stringer failure, and the panel collapsed due to skin-stringer separation after more load was applied.

8. Concluding remarks

This research analyses and tests four thermoplastic stiffened panels to investigate the damage tolerance of the welded joint.

The sensitivity studies show that the initial damage location mainly influences the skin-stringer separation initiation load for panels with one initial damage, while the final failure load is less affected. When there are two initial damages, the damage at the middle of the panel

seems critical for final failure, and the second damage location influences the skin-stringer separation initiation load.

The damage size sensitivity study considered up to a maximum damage size of 100 mm, which allowed for buckling before the start of failure. The geometrical imperfection lowers the failure load for pristine panels, while the failure load increases for panels with initial damage. Damage sizes above 40 mm show stable separation growth. This seems to delay final failure, as the initiation load decreases more compared to the failure load for larger initial damage.

Then the four panels are tested, three with initial damage and one in pristine condition. The initial damage mainly influences the failure load, with the stiffness and buckling load not considerably affected. The failure load decreased up to 16.6%, for the panel with two damages. Including a second initial damage location increases the criticality of the initial damage in the middle of the panel, as separation still seems to start from the middle location. The panel with one initial damage in the side stringer showed a lower failure load compared to the panel with initial damage in the middle stringer. This can be considered surprising, as the middle stringer is expected to attract more load and therefore be more critical for damage.

The initial damage seems to make buckling shape changes more gradually, possibly due to the opening of the damage, which can be seen on the DIC measurements. The panels with initial damage also show stable separation growth before final failure.

The panel with two initial damages showed that the middle stringer can endure a considerable skin-stringer separation event without visible damage. This can be aided by the lower load the event occurs at, leading to less load redistribution within the structure. Also, the separation event seemed to be contained by the initial damages.

The numerical analysis is able to predict the overall structural behaviour well, including the critical failure mode and initial buckling behaviour. It does, however, have difficulty predicting the buckling shape change to four half-waves, which could be due to imperfections that are not considered. The failure loads of panels with initial damage in the middle stringer are predicted conservatively, while it over-predicts the failure load of the panel with initial damage in the side stringer.

This research shows that the welded joint can withstand buckling deformation far into the post-buckling field with one or two initial damages of 40 mm. It should, however, be said that the damage size was chosen conservatively because of the unknowns concerning the weld strength at the time of manufacturing. Nonetheless, the numerical analysis showed good predictions of failure load, and predicted that panels with larger damage sizes can still withstand load into the post-buckling field. This shows great promise for thermoplastic composite primary structures, also taking into account the damage tolerance behaviour.

CRediT authorship contribution statement

Kevin van Dooren: Conceptualization, Investigation, Methodology, Software, Validation, Visualization, Writing – original draft. **Chiara Bisagni:** Conceptualization, Methodology, Project administration, Resources, Supervision, Writing – review & editing.

Declaration of competing interest

The authors declare that they have no known competing financial interests or personal relationships that could have appeared to influence the work reported in this paper.

Data availability

Data will be made available on request.

Disclaimer

The results, opinions, conclusions, etc. presented in this work are those of the authors only and do not necessarily represent the position of the JU; the JU is not responsible for any use made of the information contained herein.

References

[1] van Dooren K, Tijs B, Waleson J, Bisagni C. Skin-stringer separation in post-buckling of butt-joint stiffened thermoplastic composite panels. Compos Struct 2023;304:116294. http://dx.doi.org/10.1016/j.compstruct.2022.116294.

[2] van Dooren K, Bisagni C. Design, analysis and testing of thermoplastic welded stiffened panels to investigate skin-stringer separation in post-buckling. Composites B 2023;111033.

[3] Meeks C, Greenhalgh E, Falzon BG. Stiffener debonding mechanisms in post-buckled CFRP aerospace panels. Composites A 2005;36:934–46. http://dx.doi.org/10.1016/j.compositesa.2004.12.003.

[4] Falzon BG, Stevens KA, Davies GO. Postbuckling behaviour of a blade-stiffened composite panel loaded in uniaxial compression. Composites A 2000;31:459–68. http://dx.doi.org/10.1016/s1359-835x(99)00085-8.

[5] Paz J, Raimondo A, Bisagni C. Experimental study of post-buckled single-stringer composite specimens under fatigue loads with different load levels and load ratios. Composites B 2023;110606. http://dx.doi.org/10.1016/j.compositesb.2023.110606.

[6] Kootte L. A methodology to reproduce postbuckling in composite panels to study skin stringer separation [Ph.D. thesis], Delft University of Technology; 2023.

[7] Bisagni C, Vescovini R, Dávila CG. Single-stringer compression specimen for the assessment of damage tolerance of postbuckled structures. J Aircr 2011;48(2):495–502. http://dx.doi.org/10.2514/1.C031106.

[8] Bisagni C, Dávila CG. Experimental investigation of the postbuckling response and collapse of a single-stringer specimen. Compos Struct 2014;19:493–503. http://dx.doi.org/10.1016/j.compstruct.2013.09.018.

[9] Action J, Leone FA. Progressive damage failure analysis of a multi-stringer post-buckled panel. In: AIAA SciTech 2020 forum. (2020–1481). 2020, http://dx.doi.org/10.2514/6.2020-1481.

[10] Mo Y, Ge D, Zhou J. Experiment and analysis of hat-stringer-stiffened composite curved panels under axial compression. Compos Struct 2015;123:150–60. http://dx.doi.org/10.1016/j.compstruct.2014.11.074.

[11] Feng Y, Zhang H, Tan X, He Y, An T, Zheng J. Effect of impact damage positions on the buckling and post-buckling behaviors of stiffened composite panel. Compos Struct 2016;155:184–96. http://dx.doi.org/10.1016/j.compstruct.2016.08.012.

[12] Sepe R, De Luca A, Lamanna G, Caputo F. Numerical and experimental investigation of residual strength of a LVI damaged CFRP omega stiffened panel with a cut-out. Composites B 2016;102:38–56. http://dx.doi.org/10.1016/j.compositesb.2016.07.009.

[13] Ishikawa T, Matsushima M. Compression after impact (CAI) properties of hat stiffened CF/PEEK panels fabricated through a route without autoclave. In: Proc. 11th int. conf. on composite materials, vol. 2. 1997, p. 1–9.

[14] Orifici AC, Alberdi IOd, Thomson RS, Bayandor J. Compression and post-buckling damage growth and collapse analysis of flat composite stiffened panels. Compos Sci Technol 2008;68:3150–60. http://dx.doi.org/10.1016/j.compscitech.2008.07.017.

[15] Riccio A, Raimondo A, Di Felice G, Scaramuzzino F. A numerical procedure for the simulation of skin–stringer debonding growth in stiffened composite panels. Aerosp Sci Technol 2014;39:307–14. http://dx.doi.org/10.1016/j.ast.2014.10.003.

[16] Bertolini J, Castanié B, Barrau JJ, Navarro JP. Multi-level experimental and numerical analysis of composite stiffener debonding. Part 1: Non-specific specimen level. Compos Struct 2009;90(4):381–91. http://dx.doi.org/10.1016/j.compstruct.2009.04.001.

[17] Bertolini J, Castanié B, Barrau JJ, Navarro JP, Petiot C. Multi-level experimental and numerical analysis of composite stiffener debonding. Part 2: Element and panel level. Compos Struct 2009;90:392–403. http://dx.doi.org/10.1016/j.compstruct.2009.04.002.

[18] Ji R, Zhao L, Wang K, Liu F, Gong Y, Zhang J. Effects of debonding defects on the postbuckling and failure behaviors of composite stiffened panel under uniaxial compression. Compos Struct 2021;256:113121. http://dx.doi.org/10.1016/j.compstruct.2020.113121.

[19] Yetman J, Sobey A, Blake J, Shenoi R. Investigation into skin stiffener debonding of top-hat stiffened composite structures. Compos Struct 2015;132:1168–81. http://dx.doi.org/10.1016/j.compstruct.2015.06.061.

[20] Tijs BHAH, Abdel-Monsef S, Renart J, Turon A, Bisagni C. Characterization and analysis of the interlaminar behavior of thermoplastic composites considering fiber bridging and R-curve effects. Composites A 2022;162:107101. http://dx.doi.org/10.1016/j.compositesa.2022.107101.

[21] Tijs BHAH, Doldersum MHJ, Turon A, Waleson JEA, Bisagni C. Experimental and numerical evaluation of conduction welded thermoplastic composite joints. Compos Struct 2022;281:114964. http://dx.doi.org/10.1016/j.compstruct.2021.114964.

[22] Oliveri V, Zucco G, Peeters D, Clancy G, Telford R, Rouhi M, et al. Design, manufacture and test of an in-situ consolidated thermoplastic variable-stiffness wingbox. AIAA J 2019;57(4):1671–83. http://dx.doi.org/10.2514/1.j057758.

[23] Offringa A, van Ingen JW, Buitenhuis A. Butt-joined, thermoplastic stiffened-skin concept development. SAMPE J 2012;48(2):7–15.

[24] Tijs BHAH, van Dooren KS, Bisagni C. Development of a numerical framework for virtual testing to support design of a next generation thermoplastic multifunctional fuselage. In: II European conference on multifunctional structures. 2020, http://dx.doi.org/10.23967/emus.2020.005.

[25] NCAMP, Wichita State University. Medium Toughness PAEK thermoplastics Toray (Formerly TenCate) Cetex TC1225 (LM PAEK) T700GC 12K T1E Unidirectional Tape 145 gsm 34% RC Qualification Material Property Data Report. 2020.

[26] Abaqus 2021 documentation. Dassault Systemes Simulia Corp. 2021.

[27] Camanho PP, Dávila CG, de Moura MF. Numerical simulation of mixed-mode progressive delamination in composite materials. J Compos Mater 2003;37(16):1415–38. http://dx.doi.org/10.1177/0021998303034505.